San Jose State University

SJSU ScholarWorks

1-1-2023

Low-density star cluster formation: Discovery of a young faint fuzzy on the outskirts of the low-mass spiral galaxy NGC 247

Aaron J. Romanowsky
San Jose State University, aaron.romanowsky@sjsu.edu

Søren S. Larsen
Radboud Universiteit

Alexa Villaume
San Jose State University

Jeffrey L. Carlin
Rubin Observatory Project Office

Joachim Janz
Turun yliopisto

See next page for additional authors

Follow this and additional works at: https://scholarworks.sjsu.edu/faculty_rsca

Authors

Aaron J. Romanowsky; Søren S. Larsen; Alexa Villaume; Jeffrey L. Carlin; Joachim Janz; David J. Sand; Jay Strader; Jean P. Brodie; Sukanya Chakrabarti; Chloe M. Cheng; Denija Crnojević; Duncan A. Forbes; Christopher T. Garling; Jonathan R. Hargis; Ananthan Karunakaran; Ignacio Martín-Navarro; Knut A.G. Olsen; Nicole Rider; Bitha Salimkumar; and For full author list, see comments below

Low-density star cluster formation: discovery of a young faint fuzzy on the outskirts of the low-mass spiral galaxy NGC 247

Aaron J. Romanowsky [1,2,3]★ Søren S. Larsen [4] Alexa Villaume,[1,3,5] Jeffrey L. Carlin [6]
Joachim Janz,[7,8,9] David J. Sand,[10] Jay Strader,[11] Jean P. Brodie,[2,12] Sukanya Chakrabarti,[13,14]
Chloe M. Cheng [5] Denija Crnojević,[15] Duncan A. Forbes,[12] Christopher T. Garling [16]
Jonathan R. Hargis,[17] Ananthan Karunakaran [18] Ignacio Martín-Navarro,[2,19,20] Knut A.G. Olsen,[21]
Nicole Rider,[22] Bitha Salimkumar,[1] Vakini Santhanakrishnan,[1] Kristine Spekkens,[23] Yimeng Tang [3]
Pieter G. van Dokkum[24] and Beth Willman[21]

Affiliations are listed at the end of the paper

ABSTRACT

The classical globular clusters found in all galaxy types have half-light radii of $r_h \sim$ 2–4 pc, which have been tied to formation in the dense cores of giant molecular clouds. Some old star clusters have larger sizes, and it is unclear if these represent a fundamentally different mode of low-density star cluster formation. We report the discovery of a rare, young 'faint fuzzy' star cluster, NGC 247-SC1, on the outskirts of the low-mass spiral galaxy NGC 247 in the nearby Sculptor group, and measure its radial velocity using Keck spectroscopy. We use *Hubble Space Telescope* imaging to measure the cluster half-light radius of $r_h \simeq$ 12 pc and a luminosity of $L_V \simeq 4 \times 10^5 L_\odot$. We produce a colour–magnitude diagram of cluster stars and compare to theoretical isochrones, finding an age of $\simeq$300 Myr, a metallicity of [Z/H] ~ -0.6 and an inferred mass of $M_\star \simeq 9 \times 10^4 \, M_\odot$. The narrow width of blue-loop star magnitudes implies an age spread of $\lesssim$50 Myr, while no old red-giant branch stars are found, so SC1 is consistent with hosting a single stellar population, modulo several unexplained bright 'red straggler' stars. SC1 appears to be surrounded by tidal debris, at the end of an $\sim$2 kpc long stellar filament that also hosts two low-mass, low-density clusters of a similar age. We explore a link between the formation of these unusual clusters and an external perturbation of their host galaxy, illuminating a possible channel by which some clusters are born with large sizes.

Key words: Hertzsprung–Russell and colour–magnitude diagrams – galaxies: individual: NGC 247 – galaxies: star clusters: general.

1 INTRODUCTION

Old globular clusters (GCs) have been observed in a wide range of host galaxies to have fairly homogeneous properties that point to universal mechanisms or initial conditions for long-lived star cluster formation. For example, their typical half-light radii have a limited range of $r_h \sim$ 2–4 pc across a stellar mass range of $M_\star \sim 10^5$–$10^6 \, M_\odot$, while they host distinctive 'multiple populations' of stars characterized by variations in light element abundances (e.g. Bastian & Lardo 2018). Young star clusters with similar properties to GCs have been found in nearby star-forming regions (e.g. Larsen 2004; Brown & Gnedin 2021), with sizes that are thought to be linked to the densities of their progenitor giant molecular clouds (e.g. Grudić et al. 2021, 2022), and emerging evidence of multiple populations (e.g. Saracino et al. 2020; Li et al. 2021; Asa'd et al. 2022; Cadelano et al. 2022). Overall, a picture has emerged where bound star cluster formation is a continuous process from early times to the present

day, albeit with fewer and fewer massive GCs being formed while massive, dense gas clouds become ever rarer.

This tidy picture was disturbed by discoveries of new classes of old star clusters with more diverse properties than the classical GCs. These novelties included ultracompact dwarfs (UCDs; Hilker et al. 1999; Drinkwater et al. 2000), with typically larger sizes and luminosities: $r_h \sim$ 10–100 pc and $L_V \sim 10^7 L_{V,\odot}$. A few much fainter, large clusters ($r_h \sim$ 10–30 pc and $L_V \sim 10^4 L_{V,\odot}$) were long known in the outer halo of the Milky Way (MW), but many more were later found in dwarf galaxies, in the halo of M31 and in massive lenticular (S0) galaxies (e.g. Brodie & Larsen 2002; Huxor et al. 2005; Peng et al. 2006; Hwang et al. 2011), with nomenclatures including diffuse star clusters, extended clusters (ECs), and faint fuzzies (FFs). The lines between these classes were further blurred with the discovery of star clusters that filled the 'gap' between ECs/FFs and UCDs, with large sizes and intermediate luminosities (Brodie et al. 2011; Forbes et al. 2013).

The relations between the different star cluster families are unclear, but multiple formation pathways seem likely. Many of the UCDs are now thought to be stripped galactic nuclei (e.g. Jennings et al. 2015; Ahn et al. 2018; Mayes et al. 2021). Others may be bona

★ E-mail: aaron.romanowsky@sjsu.edu

fide star clusters whose large sizes are the product of mergers of smaller clusters (e.g. Fellhauer & Kroupa 2002). Similarly, multiple mechanisms have been proposed for the origins of ECs and FFs, including special conditions in the interstellar medium during galactic collisions (Burkert, Brodie & Larsen 2005; Elmegreen 2008), star cluster mergers (Brüns et al. 2011), expansion in the weak tidal fields of dwarfs and galaxy haloes (Madrid, Hurley & Sippel 2012) and even the effects of stellar-mass black holes (Gieles et al. 2021). Overall, ECs and FFs have received far less attention than GCs and UCDs, with little to no observational work carried out on their early formation histories or on the presence of multiple populations.

Here, we present an unusual star cluster, NGC 247-SC1 (SC1), associated with the disc galaxy NGC 247 in the nearby Sculptor group of galaxies (Fig. 1). SC1 was discovered as part of the MADCASH survey, whose goals are to study the assembly of massive dwarf galaxies through observations of their satellites, stellar haloes and GC systems (e.g. Carlin et al. 2016). From Subaru/Hyper Suprime-Cam (HSC) imaging, SC1 stood out from other known GCs around NGC 247 by its brightness and its more extended light distribution. After initially considering SC1 as a UCD, we realized that the high luminosity was largely driven by its young age (discussed below), and that by mass, the cluster should be classified as an EC or FF.

The host galaxy, NGC 247, is a borderline dwarf/giant Sd galaxy with stellar mass $M_\star \simeq 3 \times 10^9$ M$_\odot$, no bulge, disc scale length $\simeq 4$ kpc, inclination of $76°$ from face-on, disc rotation speed $\simeq 100$ km s^{-1}, halo mass of $M_{200} \sim 2 \times 10^{11}$ M$_\odot$ and specific star formation rate of $\sim 6 \times 10^{-11}$ yr^{-1} (Romanowsky & Fall 2012; Fall & Romanowsky 2018; Leroy et al. 2019; Li et al. 2020). The distance is 3.52 ± 0.10 Mpc (Tully et al. 2013), with a corresponding linear scale of 17 pc per arcsec, and 1.0 kpc per arcmin. All photometry in this paper is corrected for Galactic extinction using coefficients from Schlafly & Finkbeiner (2011), adopting the Fitzpatrick (1999) reddening law with $R_V = 3.1$, as provided by the NASA/IPAC Extragalactic Database (NED): $A_{F225W} = 0.125$, $A_{F275W} = 0.098$, $A_{F390W} = 0.070$, $A_{F475W} = 0.058$, $A_{F606W} = 0.045$, $A_{F814W} = 0.028$, $A_g = 0.057$, $A_i = 0.030$, $A_C = 0.071$, $A_M = 0.049$, and $A_{T_1} = 0.039$.

In the rest of this paper, we present spectroscopy of SC1 (Section 2), photometric observations and analysis (Section 3), photometric results (Section 4), discussion (Section 5), and conclusions (Section 6).

2 SPECTROSCOPY

We acquired optical to near-infrared spectroscopy for SC1 using the Low Resolution Imaging Spectrometer (LRIS; Oke et al. 1995) with the atmospheric dispersion corrector at the W. M. Keck Observatory on 2016 October 27, 28, and 29 (UT; program ID Y053M). LRIS has separate blue and red channels. On the blue side, we used the 300/5000 grism and on the red side we used the 600/10 000 grating, with a spectral full-width-at-half-maximum (FWHM) resolution that is strongly wavelength-dependent, from ~ 150 to 300 km s^{-1} on the blue side, to ~ 45 km s^{-1} on the red side. With this instrument setup, the D680 dichroic, and a long slit with 1 arcsec width and 3 arcmin length oriented East–West, we achieved ~ 3500–7000-Å wavelength coverage on the blue side and ~ 7800–10200 Å on the red. The total exposure time was about 2.5 h, and the airmass ranged from ~ 1.4 to 1.8.

We used the open-source Python Spectroscopic Data Reduction Pipeline version 1.4.0 (PypeIt; Prochaska et al. 2020) to do the basic data reduction. The bias level was estimated from the overscan region and subtracted from the raw data. We obtained internal flat-field images at the beginning of each night. While we did not flat-field
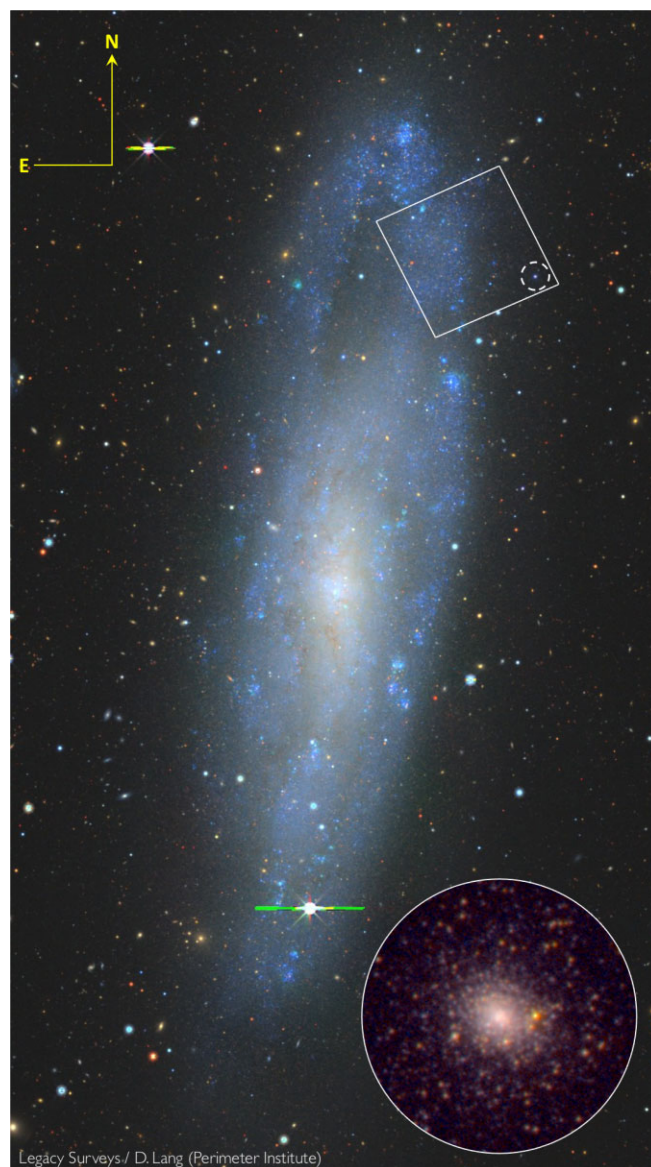

Figure 1. Overview of the star cluster SC1 in context. The larger image shows the host galaxy NGC 247 in *grz* Legacy Surveys imaging,[1] with an $\simeq 13 \times 24$ arcmin $\simeq 14 \times 25$ kpc field of view. North is up and East is left. The quadrilateral at the upper right outlines the *HST*/WFC3 footprint, with a dashed circle around SC1. At lower right is a WFC3 zoom-in on SC1 (~ 8 arcsec ~ 130 pc diameter field of view, using F475W and F606W filters), which sits 8 arcsec (8 kpc) from the centre of NGC 247 (in projection), and appears to be just beyond the outer rim of the disc.

the data for SC1, the flat-field images were used by PypeIt to trace the edges of the slit of the detector and automatically detect the object in the slit. PypeIt performs a 2D BSpline sky subtraction (e.g. Kelson et al. 2002) across the entire slit. The 1D spectra were automatically extracted using an algorithm (e.g. Horne 1986).

PypeIt wavelength calibrates the 1D spectra by calibrating on arc lamp spectra. We obtained arc frames at the beginning of each night. For wavelength calibration on the blue side, we observed the Hg, Cd, and Zn arc lamps; on the red side, we observed the Ne, Ar, Kr, and Xe arc lamps. We further optimized the wavelength solution
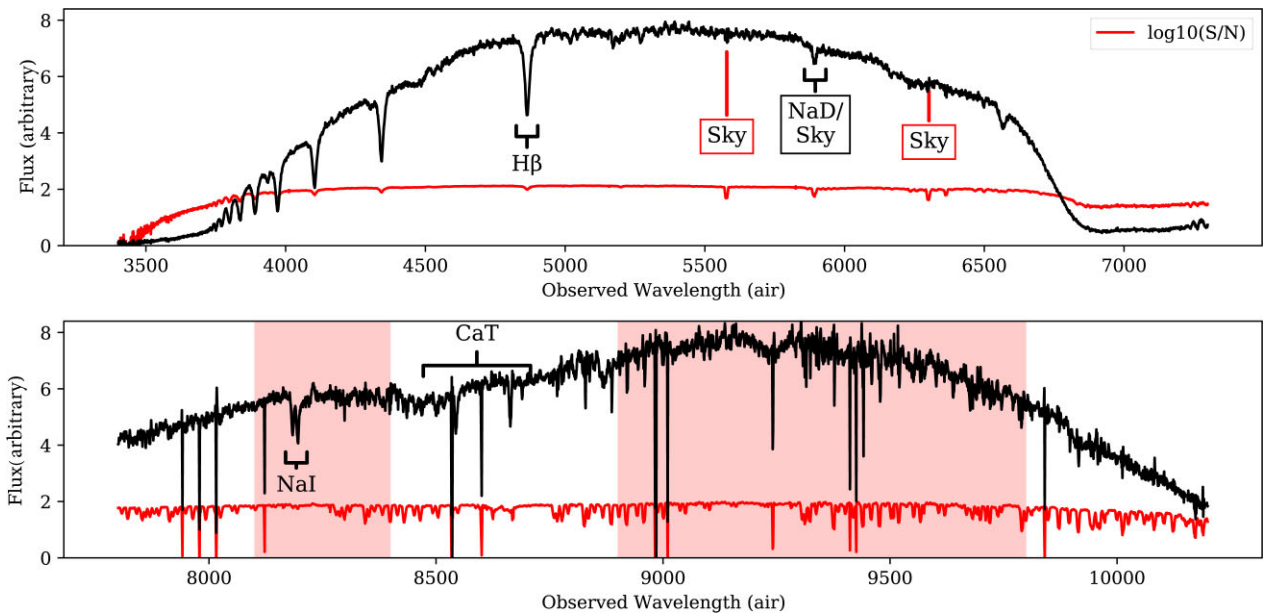
[1] https://www.legacysurvey.org/

Figure 2. The coadded, telluric-corrected LRIS spectrum for SC1 (black curves), with the blue side in the top panel, and red side in the bottom. The S/N (in log units) as a function of wavelength is shown as red curves. We highlight important spectral features, locations of sky lines and windows of significant telluric contamination. Strong Balmer lines are visible which indicate a relatively young age, and the calcium triplet is used for the redshift estimate.

by correcting the errors introduced by the varying flexure of the instrument. For the red arm, we computed how offset in wavelength the observed sky emission lines were from those in a model sky spectrum. Due to the paucity of sky lines in the region covered by the blue arm, we cross-correlated regions spanning 250 Å over the observed spectrum with a template simple stellar population to compute offsets in each region. The wavelength arrays of each arm were corrected using linear functions fitted to the respective offsets as a function of wavelength. It is possible there are still residual flexure errors at the level of $\sim$10 km s^{-1}.

We did not flux calibrate the 1D spectra. The individual exposures were coadded by weighting each exposure by the inverse variance at each pixel. The coadding also cleaned the final spectrum of cosmic rays. For the telluric correction, we followed the methodology of van Dokkum & Conroy (2012) with slight modifications, performing the correction outside of PypeIt by iterating through a grid of telluric models produced from the line-by-line radiative transfer model (Clough et al. 2005; Gullikson, Dodson-Robinson & Kraus 2014), and scaling each template to minimize the difference between it and the observed flux over the region 9320–9380 Å.

The LRIS slit captured not only the light from SC1 but also from a bright red star (hereafter 'St1') that is projected 1″0 to the West from the centre of SC1 (see zoom-in image in Fig. 1). This star will be discussed in more detail later in the paper. It is well within the total extent of SC1, which means that there is considerable overlap between the two spectra on the red side (the blue side spectrum appears to be completely dominated by SC1). Even so, with seeing of $\sim$0″9, and the extended nature of SC1, it is possible to separate the spectra in an approximate fashion by simply extracting East and West halves of the spectral trace (each with a width of eight pixels or 1″0).

We show the final spectrum of SC1 in Fig. 2 (black curves) with the blue-side in the top panel and the red-side in the bottom panel, and with some of the prominent absorption lines highlighted. We also show the wavelength-dependent signal-to-noise ratio (red; S/N; red curves) in each panel to demonstrate the high S/N achieved ($\sim$100 Å^{-1}). The Balmer lines are very strong, indicating that the

light is dominated by relatively young main-sequence stars, with ages somewhere in the range $\sim$0.1–1 Gyr. However, no emission lines are seen in the spectrum.

We use the code Prospector (Johnson et al. 2021) to determine the redshift of SC1 using the calcium triplet (CaT) region. We masked out nonphysical artefacts over the spectral ranges 8535–8540 and 8601–8606 Å. Prospector is a code for inference of physical parameters from spectroscopic data via Markov chain Monte Carlo (MCMC) sampling of the posterior probability distributions. To obtain an estimate of the posterior redshift distribution for SC1, we use a grid of theoretical stellar atmosphere models. At each MCMC step, the spectrum is shifted in velocity and the likelihood of the data given the redshift and the smoothing needed to match the grid to the data is calculated.

The heliocentric-corrected recession velocity of SC1 is 112 ± 5 km s^{-1}, confirming that it is not a background galaxy (its fuzziness in the HSC imaging already ruled it out as a foreground star). This velocity also strongly supports an association with NGC 247 as the host galaxy, which has an overall recession velocity of $\sim$150–160 km s^{-1} (NED). Spectroscopic analysis of the stellar population is planned for a follow-up paper. The same procedures with St1 return a velocity of 130 ± 5 km s^{-1}, suggesting it may be associated with SC1. We note that because the two spectra were not completely deblended, the true velocity difference may be slightly larger. There may also be systematic errors remaining in the wavelength calibration at the level of $\sim$10 and $\sim$20 km s^{-1} for relative and absolute velocities, respectively. The implications of these velocities will be considered in more detail in Sections 4.4 and 5.3.1.

3 PHOTOMETRIC OBSERVATIONS AND ANALYSIS

3.1 Subaru HSC observations

We used the HSC imager on the 8.2-m Subaru telescope (Miyazaki et al. 2012) to observe a single pointing centred on NGC 247 on 2015

October 15. The observations totalled 5040 s (16 exposures of 315 s each) in *g* band (known as 'HSC-G' at Subaru) and 2565s (9 × 285 s exposures) in *i* band ('HSC-I'). The repeated exposures were dithered translationally and rotationally to fill in chip gaps and to enable cosmic ray removal. We also took a single 30-s image in each filter to extend the dynamic range of our observations to a brighter saturation limit. The data were all obtained during photometric conditions, with seeing between 0.''55 and 0.''7 for all frames. We processed the raw data with a development version of the Rubin/LSST software pipelines, which have also been applied to HSC data (e.g. Bosch et al. 2018, 2019; Aihara et al. 2018a,b, 2019), including the removal of instrument signal, image coaddition, source detection and measurement. The results presented in this work are derived from point spread function (PSF) photometry, astrometrically calibrated to Gaia DR2 (Gaia Collaboration et al. 2018) and photometrically calibrated to the PanSTARRS-1 photometric system (Schlafly et al. 2012; Tonry et al. 2012; Magnier et al. 2013).

In order to extract photometry more optimally in the crowded environs of SC1 (and near the main body of NGC 247 itself), we ran additional PSF fitting photometry on the images that were processed by the LSST pipeline using DAOPHOT, ALLSTAR, and ALLFRAME (Stetson 1987, 1992, 1994). This extra measurement step was performed only on a single 4k by 4k 'patch' from the HSC data; crowding from stars in the outer disc of NGC 247 becomes too extreme to extract measurements just to the east of this patch. We ran two iterations of ALLSTAR, first on the original science images, then again after subtracting sources measured on the first pass to recover faint stars missed on the first iteration. We then performed forced photometry using ALLFRAME at the locations of all sources detected in either *g* or *i* bands in order to improve our photometric depth. Only sources with final ALLFRAME measurements in both *g* and *i* are kept in the final catalog. We utilize stars in common between the ALLFRAME and LSST photometric catalogues to bootstrap the ALLFRAME photometry on to the LSST calibration. The final ALLFRAME catalogue shows very good agreement with the LSST catalogue for shared sources, with a residual standard deviation of about 0.05 mag at $g = 25.5$ mag. The advantage of the ALLFRAME catalogue is that it is much more complete for regions of high stellar density, allowing us to extend our star map further to the east.

To select stars, we make use of the DAOPHOT 'sharp' parameter and the χ statistic, both of which measure deviations from the PSF model (sharp $\simeq 0$ and $\chi \simeq 1$ are good results for a point source). At the faint magnitudes of interest here ($i \gtrsim 24.5$), we find no clear demarcation in sharp and χ between the stellar locus and other objects. Therefore to help guide the selection, we use a cross-matched catalogue from the *Hubble Space Telescope* (*HST*), which has much better discrimination between stars and extended objects (see next Section). We adopt cuts based on the *i*-band imaging (with the best seeing) of $-0.5 < \text{sharp} < 0.8$ and $0.8 < \chi < 1.4$, which will reduce but not completely eliminate extended objects and blends of stars. The results using HSC star counts later in the paper (Section 5.3.1) are not sensitive to the boundaries of these cuts.

3.2 *Hubble Space Telescope* observations

SC1 was observed with *HST* as part of Program ID 14748 (PI: A. Romanowsky), on 2017 June 21 and 24, using the Wide Field Camera 3 imager with the UVIS channel. Images were taken through the F475W and F606W filters with total exposure times of 6956 and 7274 s, respectively, split into six exposures per filter (plus two shorter exposures, see below). These filters were optimised for constraining the age distribution of stars in SC1. A three-point sub-

pixel dither pattern was used (one point per orbit) with a two-point line sub-pattern (each orbit split into two exposures). The target cluster was placed near a read-out amplifier in a corner of the field in order to reduce charge transfer efficiency (CTE) losses; the opposite side of the field includes a high-density region of the host-galaxy disc (see Fig. 1).

Shorter exposures were also taken with the F225W, F275W, F390W, and F814W filters, with exposure times of ∼100–300 s each, for increased wavelength range for stellar population diagnostics using integrated light. Additional short exposures (60 s) were taken in F475W and F606W. All of the short exposures used a two-point dither pattern and post-flash illumination of 12 electrons per pixel to help with CTE losses.

The images have a pixel scale of 0.''04 (0.7 pc) and a field of view of 2.'7 × 2.'7 (2.8 × 2.8 kpc). We downloaded drc (drizzled and CTE-corrected) images from the Mikulski Archive for Space Telescopes (MAST) for the photometry. We applied extinction corrections to the photometry as given in Section 1.

In addition to these observations, we generate simulated data sets to be analyzed in parallel, in order to assess the reliability of the results and to carry out fair comparisons to models (see Larsen et al. 2011, hereafter L11). We generated artificial clusters resembling SC1 and inserted them into the F475W and F606W images, using the MKSYNTH task in the BAOLAB package (Larsen 1999). The procedure here is to draw artificial stars at random from a cluster resembling SC1 in its density profile and its stellar population. MKSYNTH models the artificial stars by considering the PSFs (derived in Section 3.4) as probability density functions, centred on the coordinates of each star, from which individual counts are drawn and added to the image. The artificial clusters were placed in relatively empty areas of the image, with a default position ∼20 arcsec to the ENE from SC1. This procedure allows us to include the effects of contamination in the analysis – both from the host galaxy and from foreground stars.

For each star, a mass was drawn randomly from a Kroupa initial mass function (IMF), and F475W and F606W magnitudes were assigned by interpolation in a PARSEC isochrone (Marigo et al. 2017)[2] with $Z = 0.004$, i.e. $[Z/H] = -0.6$, and an age of 316 Myr (log $t = 8.5$; these values will be motivated in the Section 4.1). The number of stars was adjusted to reproduce the total integrated F606W magnitude of SC1 within a 200-pixel aperture. The real and simulated F606W images are shown in Fig. 3. Note that the real image contains several bright stars, which are not present in the simulated image. These will be discussed further below. Photometry was then carried out on the simulated images in the same way as for the real images, and used in the next Sections.

3.3 Integrated light surface photometry

We measure the basic photometric parameters of the object from *HST* using cumulative aperture photometry, and report them in Table 1. This approach has the advantages of being simple and non-parametric, although there are also complications in determining the total amount of light. A correction for the 'background' level is required, which is non-trivial given the likely presence of extra-tidal debris (see Section 5.3.1). Also, the radial light profile of the cluster appears to fall off relatively slowly (see below), and extrapolating it to infinite radius does not make physical sense. We instead define a radius of 200 pixels = 8 arcsec $\simeq$ 140 pc as the edge
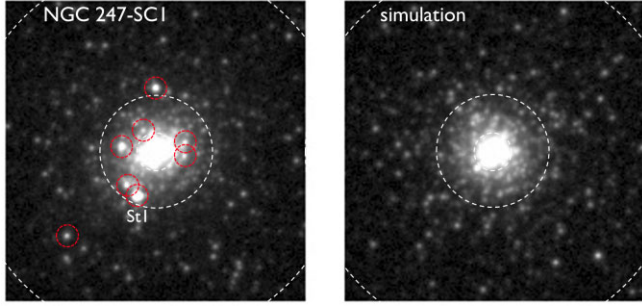
---

[2]http://stev.oapd.inaf.it/cgi-bin/cmd

Figure 3. Real (left-hand panel) and simulated (right-hand panel) WFC3 images of SC1 in the F606W filter. The field of view is 160×160 pixels $= 6\farcs4 \times 6\farcs4 = 110 \times 110$ pc. Dashed white circles (radii of 10, 30, and 100 pixels) mark the boundaries of the two annuli used for the colour–magnitude diagrams. Smaller red dotted circles in the left-hand panel mark 'red straggler' stars, with the very bright non-member star St1 labelled; one additional red straggler is outside the field of view.

Table 1. Properties of star cluster SC1. All photometry is corrected for Galactic extinction. These include the right ascension, declination, magnitudes and colours in the *HST* filters, the *V*-band absolute magnitude, the stellar mass, the half-light radius, the mean stellar surface density within the half-light radius, the axial ratio and position angle, the adopted distance and the recession velocity.

Property	Value	Units
RA	11.71154	deg J2000
Dec.	-20.65142	deg J2000
$(F606W)_0$	18.35 ± 0.02	Vega mag
$(F225W-F606W)_0$	0.40 ± 0.01	Vega mag
$(F275W-F606W)_0$	0.32 ± 0.03	Vega mag
$(F390W-F606W)_0$	0.33 ± 0.02	Vega mag
$(F475W-F606W)_0$	0.22 ± 0.01	Vega mag
$(F606W-F814W)_0$	0.33 ± 0.01	Vega mag
$M_{V,0}$	-9.28 ± 0.06	Vega mag
$M_\star$	$(8.9 \pm 0.5) \times 10^4$	$M_\odot$
r_h	11.7 ± 0.5	pc
$\Sigma_{\star,h}$	103 ± 10	$M_\odot\ pc^{-2}$
b/a	0.79 ± 0.02	
PA	54	deg
Distance	3.52 ± 0.10	Mpc
v	112 ± 5	km s^{-1}

of the cluster, which we will later see corresponds to the approximate tidal radius, and measure the sky levels from just outside this radius (200–250 pixels). We also make use of simulated cluster images (Section 3.2) to test the accuracy of our results.

We use this procedure to derive total magnitudes of $(F475W)_0 = 18.60 \pm 0.01$ and $(F606W)_0 = 18.35 \pm 0.02$, where the uncertainties are derived from the uncertain background levels. Note that for comparison to any idealized stellar population model, the expected magnitude will be uncertain at the ± 0.04 mag level owing to stochasticity (as we have found from simulating the observations). We interpolate between the two filters to the Johnson *V* band to find $V \simeq 18.45 \pm 0.02$, with an implied $M_{V,0} = -9.28 \pm 0.06$ and $L_V \simeq (4.3 \pm 0.3) \times 10^5 L_\odot$ (taking into account the distance uncertainty).

These total magnitudes should not be used for precise measurement of colour, which we have found can exhibit large, erroneous excursions from the larger apertures, probably owing to the effects of background contamination. Instead, we use an aperture of ~ 30 pixels for the colour measurement, and find $(F475W-F606W)_0 =$

0.22 ± 0.01. We also use this method to measure colours using the other filters with shorter exposures, with results reported in Table 1.

The half-light radius is derived by using the cumulative photometry within 200 pixels, and is $r_h = 0\farcs69 \pm 0\farcs03 = 11.7 \pm 0.5$ pc. Here, we adopt the average measurement from the F475W and F606W bands, and the difference between these bands as the uncertainty (which is consistent with stochastic differences in size measurements of a simulated cluster).

Note that the PSF is not taken into account in this approach, but the impact on the r_h measurement should be very minor. Also, the bright red star St1 contributes 2 and 6 per cent of the light in F475W and F606W, respectively, and since it is apparently not a member of SC1 (see Section 2), we subtracted its flux before carrying out the procedures above (which affects the F606W magnitude and the overall colour at the ~ 0.05 mag level).

We also used the aperture flux measurements to generate an F475W−F606W colour profile of SC1 out to a radius of ~ 1 arcsec, where our cluster simulation suggests variations at the ~ 0.05 mag level or more would be detectable above the stochastic background of the individual stars. We found no indication of a colour gradient at this level, and not in the other, shorter-exposure colours either.

We next use a complementary approach, the ISHAPE task for PSF-convolved and parameterized surface brightness modelling (Larsen 1999). ISHAPE is designed to model marginally resolved stellar systems, and there can be complications for a case like SC1 which is highly resolved into stars. Keeping this caveat in mind, we find the surface brightness to be well approximated by a Moffat (EFF) profile,

$$I(r) = I_0 \left[1 + (r/r_c)^2\right]^{-\eta}, \qquad (1)$$

with an envelope slope index of $\eta = 1.33$ and a majoraxis FWHM of 9.3 pixels, corresponding to $r_h = 0\farcs54$ (circularized) or 9.2 pc at the distance of NGC 247, with variations at the ~ 5 per cent level depending on the filter used and the fitting radius. Fig. 4 shows the original image, the smooth two-dimensional model and the residuals after model subtraction, where a fair number of resolved stars are visible that were effectively masked out in the fitting through a weighting function. Alternatively removing the weighting gives a larger radius: $r_h = 0\farcs63$ or 10.8 pc. The latter value is consistent with the aperture-based measurement, which we will adopt as our best estimate given the resolved nature of the system (although we take the axial ratio and position angle values from the ISHAPE fits, listed in Table 1). We note also that ISHAPE-based estimates from the HSC imaging also gave $r_h \simeq 10$ pc.

We also measure the integrated-light photometry of SC1 from HSC, using aperture photometry within a radius of $3\farcs6$, corrected by a background level within an annulus of equal area at larger radii. To capture the variations in the background, we use random quarter-circle annuli at radii between two and four times the aperture radius. We find $g_0 \geq 18.62 \pm 0.03$ AB mag and $(g - i)_0 \leq 0.37 \pm 0.04$ AB mag, where the uncertainties reflect both photometric noise and background variations, and the inequalities reflect the presence of the red star St1 which has not been de-blended in the photometry.

There is furthermore ground-based photometry available in Washington filters CMT_1 from the Mosaic II imager on the Cerro Tololo Inter-American Observatory (CTIO) 4-m telescope. This is described in Olsen et al. (2004), where SC1 was not reported in the catalogue of candidate GCs owing to its colour being too blue for an old stellar population. It has a blue magnitude of $C_0 \geq 18.72$, and colours of $(C - M)_0 \leq 0.11$ and $(C - T_1)_0 \leq 0.53$ (again with inequalities owing to the St1 blend).
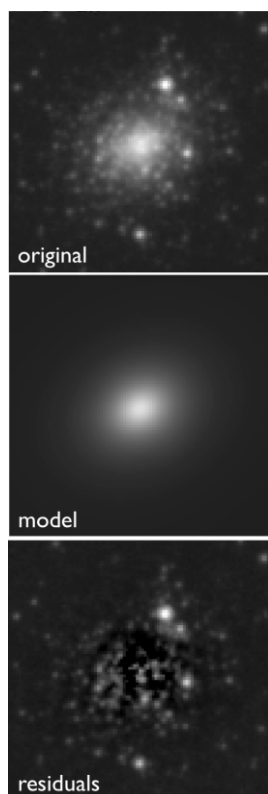
Figure 4. Modelling of the two-dimensional surface brightness profile of SC1 (F606W image) using ISHAPE. On the top is the original image, in the middle is the PSF-convolved model, and on the bottom are the residuals. The brighter point sources were essentially masked from the model fit by a weighting map.

3.4 Point source photometry

We used the ALLFRAME package (Stetson 1994) to carry out PSF-fitting photometry on the drizzle-coadded images, following a similar procedure to that described in L11. First, the FIND task in DAOPHOT was used to detect point sources in the F606W images, and a PSF was then generated for each image with the PSF task, using 20 isolated, relatively bright stars. A first pass of PSF-fitting photometry was then obtained by letting ALLFRAME measure stars simultaneously in the F475W and F606W images. In a second iteration, improved PSFs were constructed from images in which all stars except the PSF stars had been subtracted, and the FIND task was applied to the star-subtracted images to detect any sources missed in the first pass. The combined source lists were then used as input to a second pass of ALLFRAME.

The ALLFRAME photometry was calibrated to standard VEGA-MAG magnitudes by carrying out aperture photometry on the PSF stars in an $r = 5$ pixels ($0\overset{\prime\prime}{.}2$) aperture. The mean difference between the ALLFRAME and aperture magnitudes was then added back to the ALLFRAME magnitudes with an additional correction of -0.18 mag to account for the encircled flux within the reference aperture.[3] Photometric zero-points were adopted from the WFC3 pages at

STScI.[4] The photometry was also corrected for extinction, and is complete to $\sim$29 mag in both bands.

4 PHOTOMETRIC RESULTS

The overall colour of SC1 from the WFC3 imaging, $(\text{F475W}-\text{F606W})_0 = 0.22 \pm 0.01$ (Vega), corresponds to $(B-V)_0 = 0.34 \pm 0.01$, using the *HST* photometric conversion tool[5] (Sahu, Deustua & Sabbi 2014). This colour is much bluer than observed for classical old, metal-poor GCs (e.g. Reed, Hesser & Shawl 1988), supporting a young age as implied by the spectroscopy. Similarly, the CTIO Washington colour $(C - T_1)_0 \leq 0.53$ also implies an upper-limit on the age of $\sim$0.5–1 Gyr, depending on the metallicity (e.g. fig. 14 of Richtler et al. 2012). We return to more detailed consideration of the integrated colour implications later in this Section.

The remainder of this Section is structured as follows. Section 4.1 provides the core results of this paper, with analysis of the colour–magnitude diagram (CMD) of SC1 to estimate age and metallicity, while leveraging the CMD of the simulated cluster for reference. Section 4.2 compares integrated colours of SC1 to model predictions, and Section 4.3 tests for an age spread. Section 4.4 explores some unexpected bright red straggler stars, while Section 4.5 estimates the cluster mass.

4.1 Color–magnitude diagram analysis

The CMD of point sources around SC1 is shown in the left-hand panel of Fig. 5, in two different annuli (see dashed circles in Fig. 3): 10–30 pixels = $0\overset{\prime\prime}{.}4$–$1\overset{\prime\prime}{.}2 \simeq 7$–20 pc $\simeq 0.7$–2.2 r_h (blue points; at smaller radii than these, crowding becomes too severe); and 30–100 pixels = $1\overset{\prime\prime}{.}2$–$4\overset{\prime\prime}{.}0 \simeq 20$–70 pc $\simeq 2.2$–7.4 r_h (red points). Here, and for the remainder of the analysis, we adopt a cut on the photometric catalogues of $\chi < 1.5$ in F606W. This cut greatly reduces the scatter in the points from the crowded inner annulus, and has little effect in the outer annulus. We have also examined cuts using the sharp parameter, which generally rejects the same objects as χ but is less restrictive, while for the brightest stars it tends to be too restrictive. Thus, we have adopted cuts in χ only.

The right-hand panel shows the same diagram, but using a simulated data set [with $Z = 0.004$ and 316 Myr age; Section 3.2), and with the same χ cut (there are 25 contaminants in this control field, mostly with $(\text{F606W})_0 > 26.7$). It is apparent that the photometric depth of the data set is good enough to study the features of interest in the CMD, and the limiting factors will be crowding and small-number statistics of the high-mass stars. The crowding effects, even with the use of the χ cut, can be appreciated by the greater scatter in the blue than the red points in the right-hand panel, since these are all drawn from the same isochrone. In the remainder of the discussion, we will refer to the F475W and F606W filters as g and V for brevity.

PARSEC isochrone curves are also shown in Fig. 5 for reference, with $Z = 0.004$ as in the simulation, and five steps in age from 200 Myr to 10 Gyr, as labelled in the diagram; one additional isochrone is shown for $Z = 0.008$ and 251 Myr (dashed black curve). The observations show a vertical ridge in the CMD of very blue stars with $g - V \sim 0.0$ extending up to $V \sim 26$ ($M_V \sim -2$), which corresponds to the main sequence. At slightly brighter magnitudes
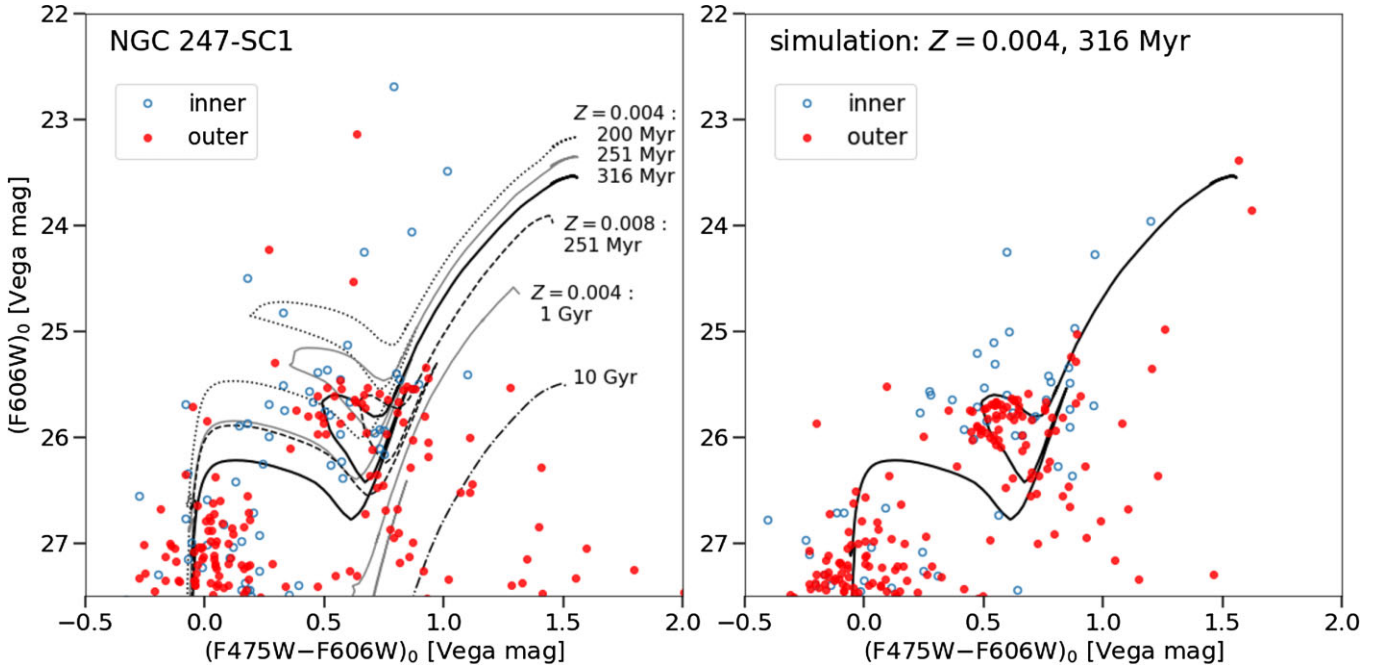

Figure 5. Colour–magnitude diagram of point sources around SC1, with left-hand panel showing the actual observations (extinction-corrected), and right-hand panel showing simulated data. Coloured circles correspond to stars selected from two different annuli, at distances of 10–30 pixels (open blue) and 30–100 pixels (filled red). Isochrones are shown at a range of ages from 200 Myr to 10 Gyr, as labelled in the diagram (grey and black curves); these all have $Z = 0.004$ except for one case of $Z = 0.008$. The observations match up well overall with the 316 Myr isochrone around both the main-sequence turn-off and the blue-loop that traces the stage of core helium burning. The simulated data set on the right uses this age and metallicity solution, with results that generally reproduce the observations on the left, both in the distributions and the numbers of the stars. On the other hand, the observations are missing AGB stars (bright and very red) predicted by the simulation, and have an excess of bright stars of intermediate colours that are difficult to explain (see main text).

and redder colours ($g - V \sim 0.4$–0.9), there is a horizontal clump of stars in Fig. 5 that corresponds to the blue loop (core helium burning supergiant phase) and matches up well with the 316 Myr isochrone, in both the zeropoints and spreads of colour and magnitude. Alternative solutions would be inconsistent with the data, as illustrated by the isochrone curves. For example, the blue loop for younger ages would be too bright and extended in colour. Adopting a higher metallicity with a younger age could match the blue-loop zero-point but would have insufficient colour spread. Similarly, a lower metallicity with older age would have too large of a colour spread.

Besides comparing to the idealized isochrone curves, we also compare to the simulated cluster corresponding to the best-matching isochrone (Section 3.2), with results shown in the right-hand panel of Fig. 5. The observed and simulated distributions are remarkably similar overall, with some differences in the brightest stars that will be discussed below. Furthermore, the absolute numbers of stars are in fair agreement, which will be discussed further below and is effectively an independent test of the solution since the simulation is normalized to reproduce the total *V*-band flux of SC1 and not the numbers of stars. Note that this comparison also provides a nontrivial test of the underlying stellar evolution models, since there have been challenges in the past with reproducing the distributions of stars along the blue loop in clusters, as well as the 'Blue Hertzsprung Gap' between the main sequence and the supergiants (see L11, and references therein).

To quantify the isochrone constraints further, we generate luminosity functions of stars selected from restricted regions of the CMD. The main sequence is isolated using a colour range $-0.5 < (g-V)_0 < 0.2$, and the observed distribution is compared in Fig. 6 (left-hand panel) to simulated observations over a range of ages. There

is a great deal of stochasticity for the very brightest magnitudes ($V_0 \sim 25$–26), owing in part to scatter of blue-loop stars into the CMD selection window. A more reliable metric is the onset of the rise in the luminosity function which begins sharply at $V_0 \simeq 26.5$ for an age of 200 Myr and more gradually at $V_0 \simeq 26.7$ for 251 and 316 Myr. The observations of SC1 are reasonably consistent with these two older ages, but not with the younger age. The expected numbers of main-sequence stars vary weakly with age and are in excellent agreement with the observed number.

Next considering the blue loop, we select stars from a box-region on the CMD that encompasses the colour range of $0.2 < (g - V)_0 < 0.95$ and the magnitude range of $V = 24.7$–27.0. We show the resulting luminosity function in the right-hand panel of Fig. 6, where the peak in the observed histogram is at $V \simeq 25.68^{+0.09}_{-0.03}$ (uncertainty from bootstrap resimulation). We compare to the simulated histograms of blue-loop star magnitudes, which show a strong age dependence of $\simeq 0.5$ mag per 0.1 dex in age, with peak magnitudes (including simulated errors) of $V \simeq 25.33 \pm 0.02$ and 25.79 ± 0.03, respectively, for ages of 251 and 316 Myr. We can thereby formally constrain the age to be $\simeq 300 \pm 10$ Myr, although the systematic uncertainties are actually much larger than this. These include the distance at the ~ 0.1 mag level and the choice of isochrones (MIST predicts the stars to be fainter by ~ 0.05 mag than in PARSEC; Choi et al. 2016). Arguably the most important factor is the potential role of stellar rotation, which could increase the brightness of the blue loop by as much as 0.7 mag (Milone et al. 2017) and thereby imply an older age. Note that the numbers of blue loop stars are expected to increase strongly with age, as shown from the simulations in Fig. 6, and are ~ 50 per cent more than observed for SC1 – which may reflect uncertainties in the models from treatments of convective
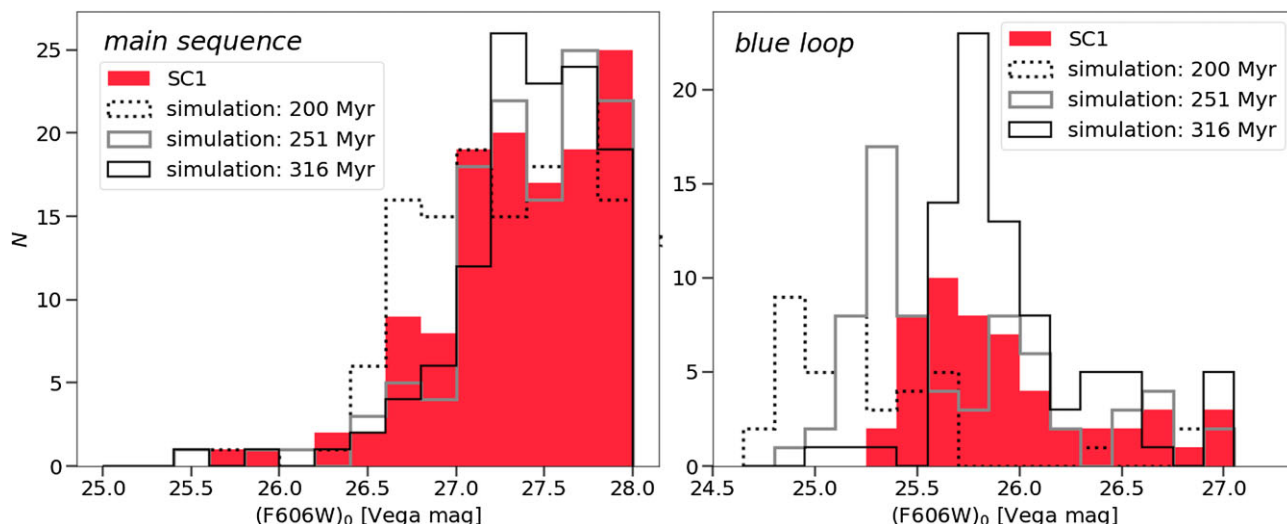
Figure 6. Distribution of star magnitudes in the outer annulus on the main sequence (left-hand panel) and from the blue loop (right-hand panel). The solid red histograms show the real observations of SC1, while the open histograms show simulated cluster observations, with different line shadings and styles indicating different ages as in the legend ([Z/H] = 0.004 in all cases). Contamination is included in all of the histograms, but should be minimal over these small areas. Both the main sequence and the blue-loop luminosity distributions in SC1 are consistent with an age of ∼300 Myr, although the blue loop is more age sensitive. The width of the blue loop luminosity peak ($\sigma_V \simeq 0.20$ mag) is consistent with the simulated peak, indicating no age spread at the level of ∼50 Myr.

overshooting, unresolved binaries and stellar rotation (Barmina, Girardi & Chiosi 2002; Costa et al. 2019).

4.2 Implications of integrated colours

A further consistency check on the age and metallicity solution is to compare the predicted global colour of the simulated cluster with the observed colour of SC1. These are (F475W–F606W)$_0$ = 0.258 ± 0.014 (where the uncertainty represents the stochasticity from 25 different simulations) and 0.22 ± 0.01, respectively, which are very close.[6] The predicted colour for a younger age and higher metallicity (250 Myr; Z = 0.008) is also almost the same – so here it is the CMD that provides the high-precision stellar population measurement. We could in principle obtain stronger constraints from the integrated light measurements by using the wider wavelength range provided by the shallower *HST* photometry discussed in Section 3.3 (see Table 1). Comparing to predicted colours from PARSEC for our CMD-based solution, the observed flux in the ultraviolet (F225W and F275W) is much too low, by ∼0.3 mag. Reasonable agreement could be obtained with older ages (e.g. ∼500 Myr) and/or higher metallicities (e.g. Z ∼ 0.008), or possibly by allowing for variations in the Galactic extinction model (e.g. with $R_V < 3.1$). However, all of these solutions would increase the F814W flux beyond what is observed. Furthermore, we have checked predicted colours from Flexible Stellar Population Synthesis (Conroy, Gunn & White 2009) and these are dramatically different from the PARSEC predictions (extremely bright in the ultraviolet). Therefore, we consider further analysis of the integrated-light colours to be beyond the scope of this paper.

---

[6]The CTIO and HSC colours are effectively slightly redder because of the presence of the embedded star St1. This led to an initial impression of a negative age gradient between the inner and outer parts of the cluster (using resolved stars from HSC), but the *HST* data now demonstrate that there is no significant gradient.

4.3 Age spread

Besides the mean magnitude of the blue-loop marking the mean age of the stars, the magnitude *width* can be translated to an age spread for the stars. The strength of this constraint is unique to the CMD approach (as compared to spectroscopy) and provided the main motivation for these *HST* observations. As shown by Fig. 6, the standard deviations of the observed and simulated peaks are similar, at $\sigma_V = 0.20 \pm 0.02$ mag and 0.18 ± 0.03 mag, respectively. Formally, this means no more than $\sigma_V \simeq 0.15$ mag spread in the underlying 'isochrones' (allowing for the uncertainties in σ_V), which translates to an upper limit of ∼50 Myr on the total age spread, or equivalently on the delay for any substantial second burst of star formation. This constraint is relatively insensitive to the systematic uncertainties discussed above in the mean age determination, and in fact also provides evidence against a large spread in stellar rotation (unless there are subpopulations with both age and rotation differences that conspire to cancel out in the blue loop magnitudes).

There is no indication of a much older population (>1 Gyr) that might be underlying a 'frosting' of younger stars. These old stars would be seen on the upper red giant branch (RGB) at $V \sim 25$–27 and $g - V \sim 1.0$. Such stars are abundant in the outer disc or halo of NGC 247, as we find in CMDs covering larger areas of the *HST* image (as will be shown in Section 5.3.1). For a quantitative comparison, there are ∼300 RGB stars in the magnitude range $V = 25$–27 in the 1600 arcsec^2 region surrounding SC1, so we expect ∼9 of these stars to appear associated with SC1 by chance. There are 13 stars observed, which is fully consistent with a projection effect plus measurement scatter from the young stars (see right-hand panel). Of course, other features (young or old) could in principle be hiding inside the central 7 pc of SC1 that are too crowded for a CMD.

4.4 Bright red straggler stars

We do not detect any candidate asymptotic giant branch (AGB) stars (brighter and redder than the blue loop) in the ∼100–300 Myr range, although the simulation shows that these would be relatively rare.

On the other hand, the observations contain three bright stars in the outer annulus (and several more in the inner annulus) that are not predicted by our preferred model solution (perhaps one or two in the inner annulus could be from photometric scatter). These stars are in the range of $V = 22.7$–24.5 and $g - V = 0.2$–1.0, and are marked in Fig. 3 as small red circles. These are generally too bright to be attributed to measurement errors or blends, according to our artificial star tests, and almost all of them have good 'sharp' values as well as good χ values. Similar objects are also very rare in the surrounding areas, and we expect only ~0.1 to appear projected on SC1 by chance. We can therefore comfortably assume that these 'red straggler' stars are associated with SC1.

In principle, the red stragglers could be blue-loop stars from younger sub-populations (~70 and ~150 Myr), but then we do not observe the corresponding blue stragglers that would be a bright extension of the main sequence. An alternative explanation is the effects of binaries that are not included in our simulations – either by appearing as unresolved, bright single stars, or by physically merging into more massive, luminous stars (see e.g. section 3.5 of L11). The latter is more realistic for providing the required brightness boost, although merger products may also be more likely to become blue rather than red stars.

A final possibility is stars leaving the AGB phase on their way to becoming planetary nebulae, the latter of which have been found in young massive clusters (YMCs; Larsen & Richtler 2006). Here, the problem is the extremely rapid (tens of years) transition time-scale expected (e.g. Miller Bertolami 2016), so that observing even one star in this phase would be unlikely, much less ~6 stars. In summary, none of the explanations for the red stragglers seems satisfactory, which underlines the utility of young star clusters for providing constraints on poorly understood aspects of stellar evolution.

Not included in Fig. 5 is the even brighter, redder star St1 with $(g - V)_0 = 1.46$, $V_0 \sim 21.42$, since our measured redshift (Section 2) indicates that it may not be directly associated with SC1. The velocity difference is 18 ± 7 km s^{-1} while the expected escape velocity of SC1 is ~5 km s^{-1}. Even so, it seems a rare coincidence that this star is so close in both position and velocity to SC1, and there may be alternative explanations. Perhaps the star was until recently a member of SC1, and is now escaping – either as a component of the surrounding tidal debris (Section 5.3.1) or through high-velocity ejection (Lennon et al. 2018) – but has not yet left the scene. In this case, the high luminosity of this star would be even harder to explain than the other red stragglers in the context of SC1. This star was also bright enough to detect in the shallow F814W imaging (called *I* band for short), which provides an opportunity for additional diagnostics using a $(g - V)$ versus $V - I$ colour–colour diagram. We estimate $(V - I)_0 \sim 2.3$–2.7 using aperture photometry. Comparing PARSEC predictions for giant-branch stars with a range of ages (to allow for stellar mergers), the observed $V - I$ colour is too red. On the other hand, a foreground main-sequence dwarf star with a metallicity of $Z \sim 0.008$ does fit the colours, suggesting the similar velocity to SC1 is simply a coincidence.

4.5 Cluster mass

To estimate the stellar mass of SC1, we try two complementary approaches. The first is to self-consistently begin with the star counts from the simulated model that matches the observations (total magnitude and CMD morphology). We sum up the initial stellar masses that are the inputs to this model, up to the main sequence turn-off mass of $3.1 \, M_\odot$, using a Kroupa IMF. We assume that all of the higher mass stars have expelled most of their mass from the cluster

and left stellar remnants, with a mean mass fraction of ~15 per cent. This leads to a model mass-to-light ratio of $M/L_V \simeq 0.21$ in Solar units, and to a final stellar mass of $M_\star \simeq (8.9 \pm 0.5) \times 10^4 \, M_\odot$. Here, the uncertainty comes from the photometric normalization and from the distance; the uncertainty in M/L from the stellar population modelling is difficult to estimate but may be comparable in magnitude.

The second approach is to use a more general stellar population synthesis model (Bruzual & Charlot 2003) to calculate the passive fading expected between the current age and ~10 Gyr in the future (assuming no stars escape the system). For an age of 316 Myr and $Z = 0.004$, this is 2.8 mag in the *V* band, leading to a future absolute magnitude of $M_V = -6.5$. If we then assume a conventional $M/L_V \sim 2$ for old star clusters, this leads to a mass of $M_\star \sim 7 \times 10^4 \, M_\odot$, which is close to the value from the first approach. The expected velocity dispersion of SC1 given its size and mass is $\sigma \simeq 2$ km s^{-1}.

5 DISCUSSION

Here, we discuss various implications of the results derived in Section 4. Section 5.1 considers how SC1 relates to other star clusters in size–mass splace. Section 5.2 connects with multiple populations and age spreads in other clusters. Section 5.3 explores the formation history of SC1 in the context of its host galaxy, along with a complex of concurrently formed material (a stellar filament and lower mass ECs). Section 5.4 summarizes general implications for the formation of low-density clusters.

5.1 Classification

Fig. 7 places the size and stellar mass of SC1 in context with *old* star clusters observed in the nearby Universe, based on the compilation of Brodie et al. (2011), with subsequent updates.[7] These literature data have *V*-band magnitudes that we convert to stellar mass with an approximate mass-to-light ratio of $M/L_V = 2$. Here it is important to recognize that there are strong selection effects in the sample, so the relative frequencies of objects in different parts of the diagram should be viewed with care, but it does provide a useful view of the range of parameter space that is known to be occupied by clusters.

SC1 resides in a well-populated region of size–mass space, in between classical GCs and the most diffuse clusters such as the Palomar clusters in the MW halo and most of the ECs in the M31 halo (Huxor et al. 2014). Other old stellar systems with similar properties include FFs in the S0 galaxy NGC 1023 (Larsen & Brodie 2000; Brodie & Larsen 2002), the MW halo clusters NGC 5053 and NGC 5466, the Large Magellanic Cloud (LMC) cluster NGC 2257, the Small Magellanic Cloud cluster NGC 339, cluster C2 in the Local Group dwarf NGC 6822 (Hwang et al. 2011), halo cluster B in M33 (Cockcroft et al. 2011) and a handful of halo clusters in M31 such as H15 and PAndAS-14. Additional, similar objects with less secure ages and distances include FFs in the interacting S0 galaxy M51B (NGC 5195; Lee, Chandar & Whitmore 2005; Hwang & Lee 2008) and diffuse star clusters in Virgo and Fornax cluster early-type galaxies (Peng et al. 2006; Liu et al. 2016). In contrast, nuclear star clusters observed in the $\sim10^5 \, M_\odot$ mass range have much more compact sizes, with $r_h \sim 1$–5 pc (Pechetti et al. 2020).

There is not an established distinction between ECs and FFs since they were discovered and named in different contexts, and

---

[7] https://sages.ucolick.org/spectral_database.html. A key asset of this catalogue is that the objects have confirmed distances.
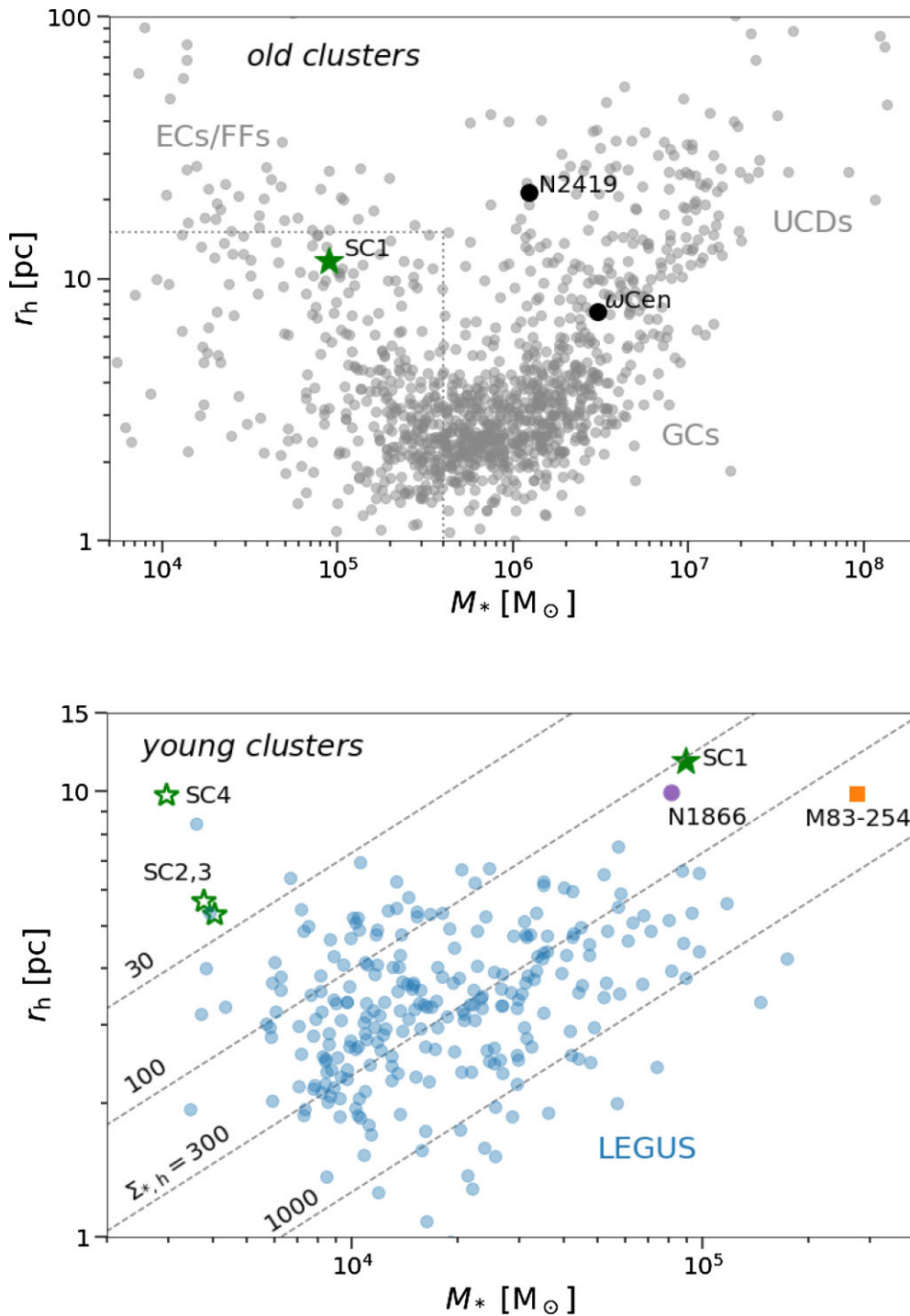
Figure 7. Compendium plots of size (projected half-light radius) versus stellar mass for star clusters. Top panel: old clusters, including GCs, UCDs, and ECs/FFs. SC1 is marked, along with several noteworthy MW objects (ω Cen, NGC 2419, and M54). SC1 is intermediate in size and mass to compact, classical GCs and the most diffuse ECs and FFs. Note that star clusters and ultrafaint dwarf galaxies (UFDs) overlap in the upper left region of this plot and are difficult to disentangle, so the data shown likely include some contamination from UFDs. Bottom panel: Young clusters with ages of ~300 Myr (note this panel is zoomed in relative to the top one, as indicated by the dotted lines). Diagonal dashed lines show constant values of effective surface density, as labelled, in units of $M_\odot$ pc^{-2}. Small blue circles show data from the LEGUS survey of nearby galaxies, as compiled by Brown & Gnedin (2021). SC1 is marked by a large filled green star symbol: it is an outlier from almost all other young clusters in the plot. The three additional low-mass star clusters (SC2, SC3, SC4; see Section 5.3.2) are marked by smaller open green star symbols; these also have relatively low densities. Other large symbols mark N5236-254 from the galaxy M83 and NGC 1866 from the LMC.

continue to be discussed independently in the literature. It does seem likely that there are two or more classes of diffuse star cluster with fundamentally different origins that happen to overlap in size–mass space. A working definition that we adopt here is that ECs are metal-poor clusters found in dwarf galaxies and in the haloes of giant galaxies, while FFs are metal-rich clusters associated with the discs of giant galaxies. With [Fe/H] ~ -1 as a very rough metallicity boundary, we then classify SC1 as an FF, which is further supported by its tentative association with the disc of its host galaxy. We note that all of the ECs/FFs with CMDs observed previously have turned out to be old and very metal-poor (e.g. Huxor et al. 2005; Da Costa et al. 2009), and hence can be classified as ECs – making SC1 the first FF with its CMD studied.

Next, we compare SC1 to star clusters of similar age in the bottom panel of Fig. 7. The primary data source is the LEGUS survey of 31 nearby star-forming galaxies, with cluster properties derived by Brown & Gnedin (2021), constituting the largest, unbiased high-quality sample of young cluster data available. We select clusters with estimated ages of 300 Myr and with 'reliable' masses and radii ($\eta > 1.3$ in our equation 1), and omit those from the galaxy NGC 1566 owing to the highly uncertain distance. The typical sizes range from ~ 2 to 5 pc at masses of $\sim 10^4$ M$_\odot$, to ~ 3 to 7 pc at $\sim 10^5$ M$_\odot$, with median stellar surface densities of $\simeq 300$ M$_\odot$ pc^{-2}. The large size of SC1 (and equivalently low density of 103 ± 10 M$_\odot$ pc^{-2}) makes it an outlier in this context.

A well-studied galaxy missing from the LEGUS sample is the giant spiral M83. One of the more extensive studies of its young clusters found that for ages of 100–200 Myr and masses of $\sim 4 \times 10^4$ M$_\odot$, the sizes are ~ 2–8 pc (Ryon et al. 2015), comparable to the LEGUS results. However, M83 also hosts a cluster that is somewhat analogous to SC1: N5236-254, with an age of $\simeq 280$ Myr, $M_\star \simeq 3 \times 10^5$ M$_\odot$ and $r_h \simeq 10$ pc (Larsen 2004; Larsen & Richtler 2006). Intriguingly, it also lies towards the outskirts of its host galaxy, at a galactocentric radius of ~ 7 kpc near the end of a spiral arm. Even so, it has a ~ 5 times higher density than SC1, similar to the lower mass clusters.

The LMC is known to host extended stellar clusters with a range of ages, although their sizes can be difficult to define owing to model fits that do not converge at large radii. Considering the sample from McLaughlin and van der Marel (2005), there is none with a comparable age to SC1 and a well-constrained large size (e.g. $\eta > 1.3$). Two that do have similar sizes and masses but different ages are NGC 2121 (3 Gyr) and NGC 1866 (100 Myr, but see the next Section with a more recent, older age estimate). The latter has a similar metallicity to SC1 and is perhaps the closest analogue; interestingly, it also may be near the tip of a stellar 'arm' of the LMC.

In summary, there are no other obvious candidates for recently formed ECs or FFs other than SC1 and perhaps NGC 1866. A possible exception is the collection of blue FFs around the S0 galaxy NGC 1023 (Forbes et al. 2014). These may be young clusters, or they may be old and metal-poor: more detailed observations would be required for confirmation.

The properties of the star cluster system of NGC 247 itself are also relevant for putting SC1 in context. The galaxy is relatively sparse in YMCs, which appears to be a natural reflection of its low star formation rate (Larsen & Richtler 2000). Sizes were estimated for a few of these from ground-based data (Larsen 1999) but will need revisiting with higher-resolution imaging. The old GC system remains relatively understudied, with Olsen et al. (2004) having confirmed three clusters spectroscopically, although there may be as many as ~ 60 GCs total. These three clusters are all consistent with fairly high metallicities ([Fe/H] ~ -1.0 to -0.6), old ages, and sub-solar α-element abundances. They are projected at or just beyond the edge of the galactic disk, and appear to co-rotate with the disc. Analysis of the HSC imaging indicates that these three are compact rather than ECs like SC1 (Santhanakrishnan 2016).

5.2 Multiple stellar populations

Multiple populations are a long-standing mystery in star clusters. While old GCs are well approximated by coeval stars of a single age and metallicity, they also show pervasive peculiarities in the star-to-star variations in light elements. Most proposed explanations involve a second generation of stars that form from material enriched by the first generation, on time-scales of anywhere from ~ 1 to ~ 50 Myr. Unfortunately, none of the explanations to date fits comfortably with the many constraints provided by observations (see review by Bastian & Lardo 2018).

Multiple populations have been generally detected in clusters down to ages of ~ 2 Gyr, but not younger (Cassisi & Salaris 2020) – which is a major puzzle since there is no reason for the underlying physics or initial conditions to change for that age. The suspicion has been that this incongruity reflects an observational limitation, for example, by studying stars on the RGB rather than the main sequence, which seems to be confirmed by recent observations (Cadelano et al. 2022). If YMCs do host ubiquitous multiple populations, they then serve as important test-beds for the presence of age spreads which could be closely linked to abundance spreads.

In this vein, younger clusters do show widespread peculiarities in their CMDs, such as extended main-sequence turn-offs (e.g. Mackey et al. 2008; Milone et al. 2009; L11). These were initially interpreted as age spreads of up to a few hundred Myr, but now appear more likely driven by other processes such as stellar rotation and mergers (e.g. Bastian & de Mink 2009; Niederhofer et al. 2015; Milone et al. 2018; Kamann et al. 2020; Wang et al. 2022). Even so, rotation variations may connect to abundance variations in young clusters (Pancino 2018). Furthermore, there are still signs of age spreads in some cases (Goudfrooij, Girardi & Correnti 2017; Costa et al. 2019; Gossage et al. 2019), which motivates a wider inventory of CMDs in YMCs.

SC1 represents a significant addition to the literature on CMD variations – as a young, high-mass cluster with a low density and a different formation environment from clusters studied in the MW and its satellites.

Our ~ 50 Myr upper limit on its age spread is in tension with the extended star formation histories required in AGB-polluter scenarios (D'Ercole et al. 2010), although the low escape velocity of SC1 already makes it unlikely to retain stellar ejecta. As discussed in Section 4.3, we also can exclude significant spreads in stellar rotation. Whether or not this cluster is completely free of multiple populations could be tested further with integrated light spectroscopic analysis of its abundances such as sodium.

The LMC cluster NGC 1866 provides an intriguing comparison to SC1, since its age, mass and size make it a potential analogue to SC1 (see Section 5.1). This well-studied benchmark young cluster has a split main sequence that may reflect a combination of rotation and age variations (Dupree et al. 2017; Milone et al. 2017). Costa et al. (2019) analyzed a sample of Cepheids in this cluster and concluded that the stellar population overall most likely consists of a dominant fast-rotating population with an age of $\simeq 290$ Myr, and a secondary, relatively slow-rotating population with an age of $\simeq 180$ Myr. (along with small differences in the metallicity of [Fe/H] ~ -0.4). The fast-rotating stars may be understood as inheriting angular momentum from their initial gas cloud, but it is not understood how the cluster would re-ignite a second population. Here we present a new puzzle
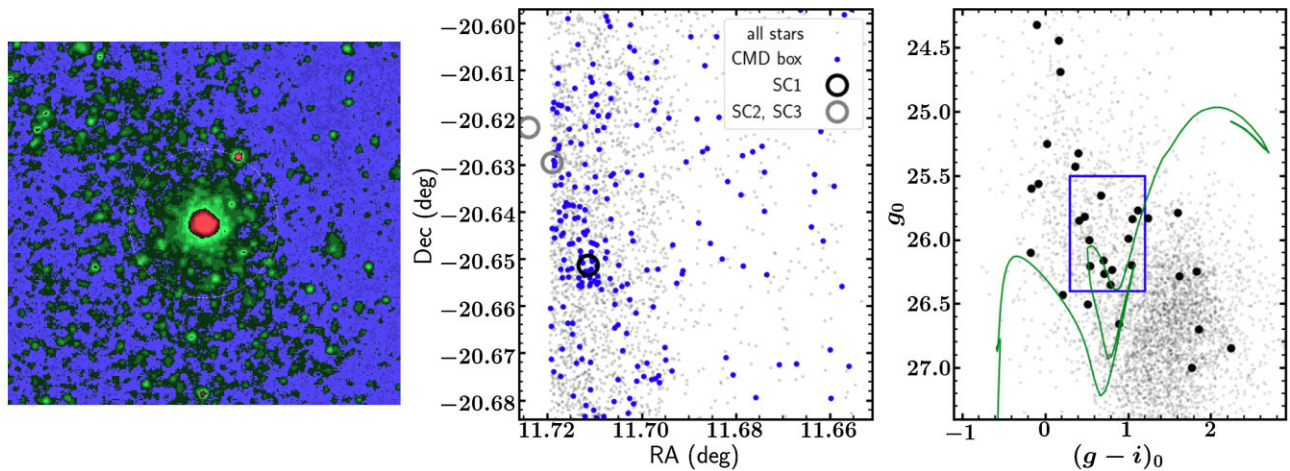
Figure 8. Filamentary feature extending through SC1, as seen in the HSC data. North is Up, and East is left. Left-hand panel: *g*-band image displayed with false colour for the sake of contrast, where the dotted circle marks the expected $\simeq 9$ arcsec tidal (150 pc) radius. There appear to be broad linear features extending outwards from just inside the tidal radius. Middle panel: Spatial positions of star counts, where small grey dots show all stars and larger blue circles show 'blue loop' stars. The position of SC1 is marked by an open black circle, from which a linear feature in the star counts is seen to extend $\sim 0.03°$ (~ 2 kpc) towards the Northeast. The *HST* image barely captures the filament but does not extend far enough to the West and South to pick up the density contrast with the surrounding regions (see Fig. 1). Two low-mass clusters (SC2 and SC3) are marked by open grey circles. The disc of NGC 247 begins at the left-hand side of this plot, where crowding makes individual star photometry challenging (hence the 'empty' region). Right-hand panel: CMD of a ~ 50 arcmin^2 region in the halo of NGC 247 (grey dots). The black points show stars selected within 10 arcsec of SC1. The green isochrone curve shown is for an age of 300 Myr and metallicity of $Z = 0.004$. The blue rectangle shows the selection box used for blue-loop stars that are plotted in the middle panel.

of why the similar cluster SC1 does not likewise present evidence for multiple generations of stars.

5.3 Host galaxy context: filament and low-mass clusters

5.3.1 SC1 orbit and stellar filament

Given the proximity of SC1 in projection to the outer rim of the disc of NGC 247 (Fig. 1), we would like to know if there is a current or past physical connection. Velocity is one potential clue, to test if an object is corotating with the disc or is on a more random, halo-like orbit. We use publicly available data from the VLA-ANGST survey (Ott et al. 2012) to map out HI emission around NGC 247. The cold gas disc of the galaxy extends out almost to the position of SC1, with a projected separation of ~ 20 arcsec ~ 350 pc. The HI velocity range in this area is $\simeq 80$–100 km s^{-1}, and the Hα emission velocities appear similar (Hlavacek-Larrondo et al. 2011), in both cases close to the SC1 velocity of 112 ± 5 km s^{-1}.[8] An association between cluster and disc appears possible (similar to the apparent co-rotation of the three known GCs), although SC1 may also be on a more random orbit whose line-of-sight velocity just happens to be similar to the disc's (we revisit gas associations below). If we assume SC1 is in the disc plane with an inclination of 76°, we can deproject its position to give its true galactocentric distance as $r_G \simeq 14$ kpc.

This inferred distance allows us to calculate the expected tidal radius r_t for SC1:

$$r_t = \left(\frac{GM r_G^2}{2v^2} \right)^{1/3}, \qquad (2)$$

where M is the cluster mass and v is the circular velocity of the host (see Baumgardt et al. 2010). With $v \simeq 110$ km s^{-1} (Lelli, McGaugh & Schombert 2016; Ponomareva, Verheijen & Bosma 2016), we find $r_t \simeq 145$ pc $\simeq 8\farcs5$. If SC1 is not actually in the disc plane, and we allow for a wider range of plausible distances $r_G \sim 10$–25 kpc, this leads to $r_t \sim 120$–220 pc ~ 7–13 arcmin.

Given the extended nature of SC1 and its relative proximity to its host galaxy, we next test for indications of extra-tidal stars or other non-equilibrium features. Visual inspection of the HSC *g*-band imaging suggests the cluster stays relatively round and asymmetric out to ~ 5–6 arcsec ~ 100 pc, but beyond this radius shows signs of broad, extended features to the Northeast and Southwest (see left-hand panel of Fig. 8). This transition is suggestive of a slightly smaller tidal radius than our default value, which may in turn imply that SC1 is at a distance of $r_G \sim 8$ kpc and is *not* associated with the disc. This smaller distance would imply the cluster is well out of the disc plane into the inner halo, at a height of ~ 3 kpc.

The south-west feature appears to terminate fairly sharply at a distance of ~ 25 arcsec (~ 400 pc), while the Northeast feature extends a much longer distance of ~ 2 arcmin ~ 2 kpc, with a width of roughly ~ 15 arcsec ~ 250 pc, until it overlaps with the disc. Thus it appears that SC1 is located around the end of a stellar filament that could be a tidal stream or a very faint spiral arm.

For more precise mapping out of the filament, we turn to star counts from HSC (Section 3.1), using the stars associated with SC1 (within a radius of 10 arcsec) to motivate a colour–magnitude selection area for the filament (see right-hand panel of Fig. 8). This procedure assumes that the stellar populations in the filament and the cluster are similar, which will be tested further below. We use colour and magnitude ranges of $(g - i)_0 = 0.3$–1.2 and $g_0 = 25.5$–26.4, respectively, which correspond approximately to the empirical blue-loop region. The spatial distribution of these 'blue-loop' stars is shown in the middle panel of Fig. 8, which shows a narrow, linear feature extending to the north-east of SC1 and confirms the visual impression from the original image. If the selection box is moved to bluer or redder
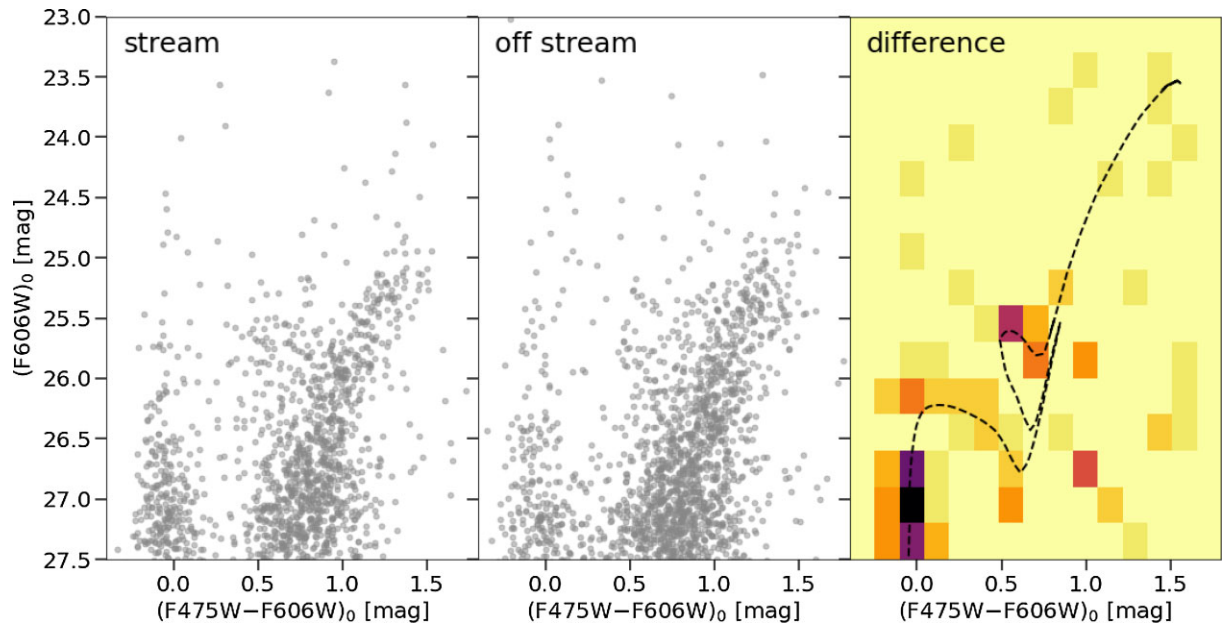
---

[8] As discussed in Section 2, this velocity uncertainty may be underestimated, and indeed preliminary analysis of a lower S/N but higher resolution spectrum from Keck/HIRES suggests a value of $\simeq 95$ km s^{-1}.

Figure 9. CMDs of point sources from 0.5 arcmin^2 regions of the *HST* image. Left-hand panel: filament associated with SC1. Middle panel: off-filament area to the East. Right-hand panel: on/off filament difference, expressed as a Hess diagram, where darker shading represents higher densities. The dashed curve shows the $Z = 0.004$, 316 Myr isochrone that matches the SC1 data (Fig. 5). The filament contains an excess of both blue-loop and main-sequence stars, whose locations in the CMD are consistent with SC1.

colours (e.g. capturing RGB stars), then the density map no longer shows the filamentary feature. The stellar population of this feature will be examined below in more detail using *HST*, while here we test the statistical significance of the Southern truncation using HSC with its larger field of view. We place 740 arcsec^2 rectangular apertures along the filament, finding that the number of blue-loop stars remains constant at 15–16 until the truncation is reached at ~25–30 arcsec from the centre of SC1. Beyond this point, the number in the aperture is 1–3 stars, i.e. a decrease at the 3σ level.

We next check multiwavelength archival imaging from NED for any other signs of the filament. It does appear to be detected but ill-defined in CTIO *B*-band imaging from the *Spitzer* Local Volume Legacy survey (Cook et al. 2014). Similarly, it is marginally visible in luminance-filter imaging (Rich et al. 2019). In *GALEX*, there appears to be slight excess emission roughly in the same area as the filament, both in FUV and NUV, but it may not be well aligned with the HSC feature (in contrast, SC1 itself is a strong ultraviolet source).

We also revisit the VLA data to search for lower density gas around SC1 and the filament. We do indeed detect signs of widespread gas not reported in previous HI observations, but at faint levels that are difficult to map out over large spatial scales given the minimum VLA baseline, and there is no clear detection of a linear feature associated with the stellar filament. We find typical gas mass densities of M_{HI} $\sim 2 \times 10^6$ M$_\odot$ kpc^{-2}, at velocities of $\simeq$50–100 km s^{-1}. This fairly uniform gas distribution at disc-like velocities most likely represents an extension of the disc, with any remaining cold gas associated with the filament either present at a lower mass level or dispersed to other parts of the galaxy. Star formation rates at these low densities in outer discs are expected to be extremely low, $\Sigma_{SFR} \sim 2 \times 10^4$ M$_\odot$ Gyr^{-1} (Bigiel et al. 2010), so these gas detections should not represent the formation sites for SC1 and the stellar filament – although there is precedent for the apparent formation of massive star clusters in the low-density outskirts of M83 (Dong et al. 2008).

The *HST* imaging is less effective for capturing the density contrast between the filament and the surroundings, owing to the smaller field

of view, although the filament is detectable in carefully smoothed maps of young star counts, particularly close to SC1. Instead, *HST* is most useful for examining the stellar population of the filament in detail, as shown by Fig. 9. Here, we have selected equal areas of the *HST* image (0.5 arcmin^2), both on (left-hand panel) and off (middle panel) the filament (immediately to the East). The differences between the panels are subtle, as both fields show a dominant RGB population as well as a main sequence extending to bright magnitudes. The filament field does show a modest excess of stars in the blue-loop region at $(g - V)_0 \sim 0.7$, $V_0 \sim 25.7$.

To view the differences more clearly, we construct a Hess CMD binned-density diagram of each of the two fields and then subtract them in order to generate a difference map (right-hand panel). Here, we display negative values as zero (light yellow) in order to avoid being dominated by the radial gradient in RGB density. Two primary features emerge that are insensitive to the binning scheme: an excess of main-sequence stars at $V \sim 26$–27.5, and an excess of blue-loop stars. The locations of these features in the CMD are very similar to those of SC1 – as can be seen by using the isochrone curve as a reference, and as we have confirmed from examining their luminosity functions and comparing to Fig. 6. To test the statistical significance of this result, we carry out 25 bootstrap resampling iterations of the two fields, and find that in every case, the Hess diagram shows a clear overdensity along the SC1 isochrone. These features also confirm the result from the HSC data (Fig. 8) that the filament consists of a population of young stars with no sign of underlying old stars. There are also hints of an excess of red straggler stars along the filament and in the general vicinity of SC1, but the numbers are too low to be sure.

To estimate the stellar mass of the filament, we use stars from the upper main sequence and the blue loop as tracers, calibrating the ratios between these stars and total stellar mass using the outer annulus of SC1. Over a filament area of $\simeq$0.7 arcmin^2 $\simeq$ 0.7 kpc^2, we use this approach (after correcting for background levels) to find $M_\star \sim 10^4$ M$_\odot$, i.e. a factor of ~10 less massive than SC1. The
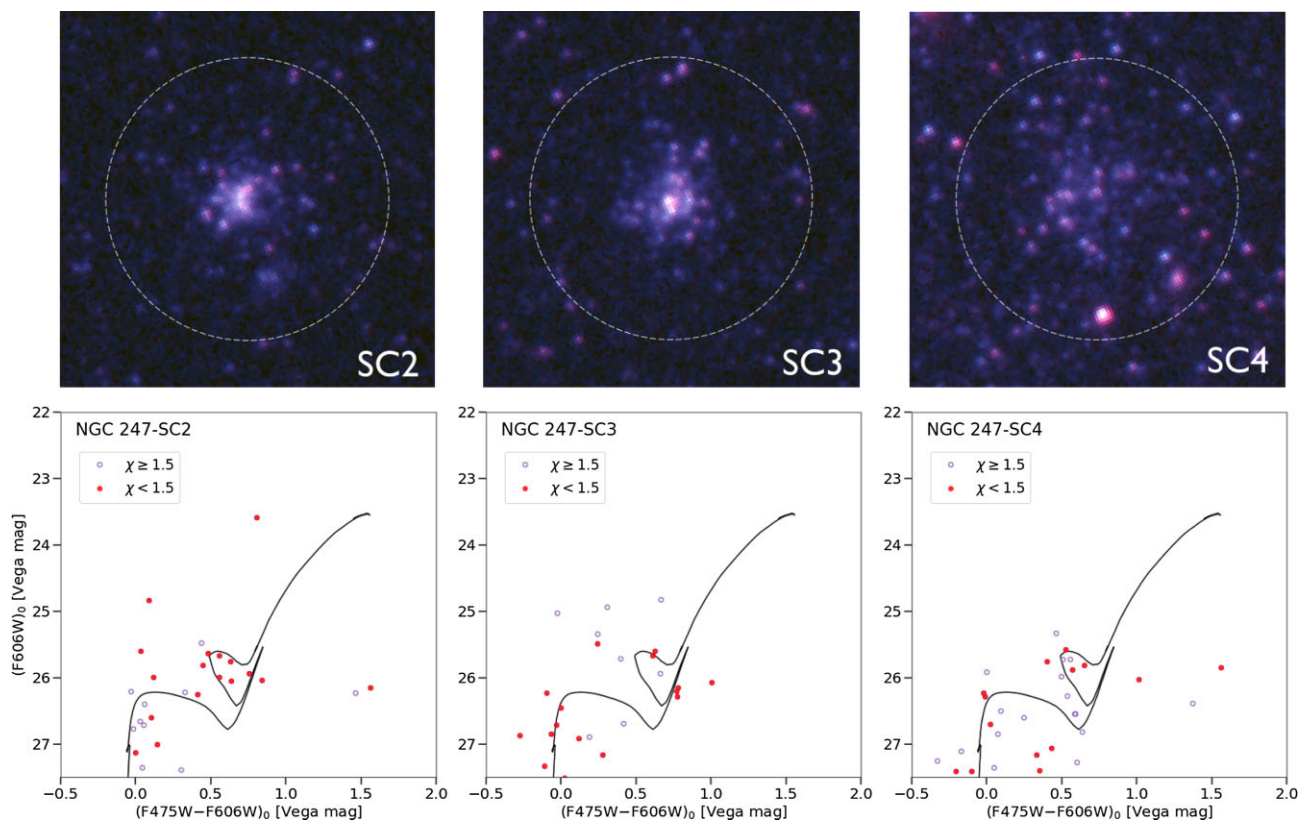
Figure 10. Low-mass clusters SC2, SC3, and SC4 (left- to right-hand panels) identified in *HST*/WFC3 imaging. Top panels show colour thumbnails using the F475W and F606W filters. North is up and East is left. Large dotted circles are drawn for reference, with a radius of $1''.8 \simeq 31$ pc. SC2 and SC3 are in the filament extending northwards from SC1. SC4 is in an outer section of the host galaxy disc. Bottom panels show the CMDs for the clusters within a radius of $0''.8 \simeq 14$ pc, using the same axis ranges as in the SC1 CMD in Fig. 5. The higher and lower quality measurements are indicated by red filled and open purple circles, respectively. The curves show a 316 Myr, $Z = 0.004$ isochrone, which appears consistent with the data for all three clusters. Nearby control fields of similar areas would show only $\sim$3 stars in the CMD in the cases of SC2 and SC3, and $\sim$12 stars in the case of SC4 (most of these away from the isochrone).

equivalent surface brightness is $\mu_V \simeq 29.4$ mag arcsec^{-2}, which is at or beyond the limit of the very deepest studies of extragalactic streams in integrated light (see summary in section 3.3 of Duc et al. 2015). After 10 Gyr of fading, and if still intact, the filament would have $\mu_V \simeq 32$ mag arcsec^{-2}, and any such features in the haloes of galaxies beyond the Local Group would be essentially undetectable.

5.3.2 Low-mass star clusters

We next carry out an initial search for more star clusters that may be coeval with SC1, since star clusters normally form together in a cohort with a characteristic mass distribution (e.g. Larsen 2009). SC1 is near the characteristic upper-mass cutoff of this distribution, and thus we expect many more lower mass clusters to have formed – although after 300 Myr, many of them may have been disrupted or else diverged in their orbits to different parts of the galaxy. We search for clusters in the Western half of the *HST* image (away from the galaxy disc), both by eye and by using star counts, using a CMD box to select blue-loop stars as done with the HSC data, and now with box boundaries of $(g - V)_0 = 0.35$–0.85 and $V_0 = 25.4$–26.7 mag. There are three obvious clusters of stars, all of them toward the NNE of SC1, at distances of $1'.4$–$2'.4 = 1.4$–2.4 kpc (see thumbnail images and CMDs in Fig. 10). Two of these appear to be embedded in the filament (see the right-hand panel of Fig. 8), and one is in a protrusion of the NGC 247 disc near the 'top' of the filament. In

the HSC imaging, they would be much more difficult to identify, as small smudges with more stochastic global colours.

We dub the three low-mass clusters SC2, SC3, and SC4, in order of proximity to SC1, and summarize their properties in Table 2. Here, we have used aperture-photometry profiles to derive their *HST*-based total magnitudes, colours and sizes, as done for SC1 in Section 3.3, but now with a maximum radius of 30 pixels ($1''.2$). Their colours are all consistent with that of SC1, as expected for a coeval population. We have also derived HSC g, i photometry using the procedures described in Section 3.3, although we had to use a small $1''.8$ aperture for SC4 to avoid including flux from nearby bright stars.

To derive the cluster masses, we assume the same $M/L_V = 0.21$ as for SC1. We plot their sizes (5–10 pc) and masses (3000–4000 M$_\odot$) in the bottom panel of Fig. 7, where they appear as relatively low-density clusters (5–20 M$_\odot$ pc^{-2}), at the upper size envelope of the LEGUS distribution, although this survey may be incomplete for such clusters. Analogous clusters in the Local Group with old ages are Pal 4, M33-D and PAndAS-45. We calculate expected tidal radii as done above for SC1, assuming $r_G \sim 10$ kpc, and find that they all have $r_t \sim 40$ pc $\sim 2''.3$. This means that the clusters should not be in imminent danger of disrupting, and in the cases of SC2 and SC3 there are no obvious indications of extra-tidal material. The very low density cluster SC4 appears to be particularly asymmetric, and its boundaries are unclear since it is embedded in the disc. This object seems the most likely to disrupt soon, although its location in the disc may also be only a projection effect.

Table 2. Properties of low-mass star clusters around NGC 247 – see Table 1 for details of columns.

Name	RA (J2000)	Dec. (J2000)	$(F606W)_0$ (Vega mag)	$(F475W-F606W)_0$ (Vega mag)	g_0 (AB mag)	$(g-i)_0$ (AB mag)	M_V (Vega mag)	$M_\star$ ($M_\odot$)	r_h (pc)
NGC 247-SC2	11.7191	−20.6295	21.86 ± 0.05	0.17 ± 0.05	21.85 ± 0.13	−0.14 ± 0.25	−5.82 ± 0.08	3800 ± 200	5.7 ± 0.5
NGC 247-SC3	11.7240	−20.6221	21.77 ± 0.05	0.23 ± 0.05	21.66 ± 0.20	0.58 ± 0.23	−5.90 ± 0.08	4000 ± 200	5.3 ± 0.5
NGC 247-SC4	11.7348	−20.6190	22.05 ± 0.20	0.29 ± 0.20	22.53 ± 0.21	0.31 ± 0.29	−5.55 ± 0.21	2900 ± 600	9.8 ± 1.7

The existence of these low-mass clusters along the filament reinforces a picture where all of this material including SC1 is connected, and originated in the same star-forming event. An alternative scenario where the filament represents tidal material lost from SC1 is undermined by the very strong asymmetry of the filament relative to the cluster (i.e. missing either the leading or the trailing tidal tail, which would be very hard to hide in projection).

5.3.3 Connections to galaxy disturbances

While this filament has not been previously reported, there are other signatures of disturbances in the recent history of NGC 247. An ∼3 kpc 'void' in the Northern half of the galaxy was examined in detail by Wagner-Kaiser et al. (2014) and suggested as the imprint of a nearly dark subhalo impact. Davidge (2021) subsequently mapped out the large-scale multiwavelength properties of the galaxy and determined that the void is an illusion created by an overluminous spiral arm on the Northern edge of disc, which, in turn, was most likely provoked by an external perturbation. This would have occurred within the last few dynamical times of the disc, which is ∼100–300 Myr. There are also large bubble-shaped regions of young stars in the disc with estimated expansion ages of ∼150–250 Myr (Davidge 2021). The galactic nucleus appears to have experienced a starburst ∼100–300 Myr ago (Kacharov et al. 2018). All together, it appears there was a galaxy-wide disturbance ∼300 Myr ago that continued until ∼100 Myr ago, followed by a period of relative quiescence (NGC 247 is now ∼1σ below the star-forming main sequence; Leroy et al. 2019).

The 300 Myr age of SC1 coincides with the beginning of the galaxy disturbance and suggests a link between the two – with SC1 being either the culprit or a by-product of the event. Its orbital period is likely in the range of ∼0.5–1 Gyr, so it is plausible that SC1 was born in or near the galaxy disc 300 Myr ago, before travelling to the present position. The ∼$10^5 M_\odot$ stellar mass in SC1 is too low to induce the large-scale disturbances in the host galaxy, considering the disc mass is $M_\star \sim 3 \times 10^9 M_\odot$. For SC1 to be responsible, there must have been a lot more accompanying material – either in dark matter or in gas – that is not observable now.

We thus consider first a conventional minor merger scenario involving a disrupting satellite galaxy, analogous to the Sagittarius dwarf interaction with the MW (e.g. Purcell et al. 2011; Ruiz-Lara et al. 2020). The lower mass of the host galaxy, NGC 247, would then imply a much fainter satellite galaxy perturber, given the steep stellar-to-halo mass relation for dwarf galaxies (e.g. Wechsler & Tinker 2018). A dark subhalo mass of ∼$10^8 M_\odot$ has previously been suggested for producing the void in NGC 247 (Wagner-Kaiser et al. 2014; see also Kannan et al. 2012; Shah et al. 2019). This would be the mass at impact, while the mass at infall before tidal stripping of the dark matter halo would be ∼$10^9 M_\odot$. Expectations for stellar masses in this regime are an area of active research and still very uncertain, but current estimates are in the range of ∼10^3–$10^5 M_\odot$ (Wheeler et al. 2019; Applebaum et al. 2021), i.e. an UFD.

A relevant observational example of a satellite system is NGC 2403: another nearby galaxy from the MADCASH survey with comparable mass and morphology to NGC 247. It has two known satellites, DDO 44 and MADCASH-1 (Carlin et al. 2019, 2021), the former of which is disrupting, with stellar masses of 2×10^7 and $2 \times 10^5 M_\odot$, respectively. Either of these would have more than sufficient halo mass to produce the disturbances in NGC 247 (which incidentally raises the question of why NGC 2403 appears unscathed despite the recent pericentric passage of DDO 44). Another example is the irregular dwarf NGC 4449 whose starbursting activity was unexplained until the discovery of a disrupting dwarf around it with a stellar mass of $2 \times 10^7 M_\odot$ – a so-called stealth merger (Martínez-Delgado et al. 2012). These satellites are generally more massive than required for the NGC 247 disturbances, but illustrate the idea that external perturbers can easily evade detection.

We are not aware of any satellite galaxies around NGC 247 — other than two fairly massive ones that will be discussed below – nor of any other tidal features in either gas or stars (Westmeier et al. 2017; Rich et al. 2019). However, a UFD could have been missed – almost certainly so if it were disrupted (recall that SC1 would not be a direct remnant of the satellite, owing to the single-burst recent star formation history and to its off-centre location in the filament.) SC1 and the associated stellar filament and low-mass clusters might then have formed either from disc gas from NGC 247 flung out after impact – a 'galactic feather' scenario (Laporte, Johnston & Tzanidakis 2019; Martinez-Delgado et al. 2021) – or from cold gas belonging to the UFD.

There are indications that UFDs can retain gas in the field even if they quench very early (Janesh et al. 2019; Applebaum et al. 2021), and perhaps they can also avoid ram-pressure stripping during infall to a low-mass galaxy. If the precursor to SC1 harboured at least ∼$10^6 M_\odot$ of cold gas, this could have been compressed during disc passage to form a massive cluster along with a train of stars and lower mass clusters. An analogous case is the unique object Price-Whelan 1 (PW 1): a young (∼120 Myr) open cluster far out in the MW halo (Price-Whelan et al. 2019), which is thought to have formed from gas in the leading edge of the Magellanic stream around the time of disc crossing (Bellazzini et al. 2019). PW 1 is actually composed of at least three sub-clumps with masses of $M_\star \simeq 200$–700 $M_\odot$ and sizes of $r_h \simeq 30$–120 pc – i.e. with even lower densities than SC1 and its associated clusters (see again Fig. 7). Despite the similarities, though, there is a dramatic difference in outcomes between just ∼$10^3 M_\odot$ of stars forming from $3 \times 10^7 M_\odot$ of gas (Brüns et al. 2005) in the case of PW 1, and ∼$10^5 M_\odot$ in the case of SC1 and its likely less massive gas reservoir.

To distinguish between the above two possibilities – star formation from gas in the disc versus gas in the satellite – we may consider the [Z/H] $\simeq -0.6$ metallicity of SC1. The disc metallicity for young stars (∼15–40 Myr) was determined to be [Z/H] ~ -0.3 based on the colours of red supergiant stars from ground-based imaging, and with little variation with galactocentric radius (Davidge 2006). The ∼0.3 dex difference between these two measurements may not be meaningful given the statistical and systematic uncertainties.

Estimating the disc metallicity from the area covered by our *HST* pointing would also be a challenging exercise beyond the scope of this paper. For now, we consider the approximate match in metallicity to be indicative of a disc-related origin for SC1. For example, a UFD origin would lead to a much lower metallicity between [Z/H] ~ -3 and -2 (Simon 2019), unless there was some mixing between UFD and disc gas (cf. Tepper-García & Bland-Hawthorn 2018).

We consider next an alternative scenario, of a pure gas cloud with no dark matter that interacted with the disc of NGC 247 and triggered its own internal burst of star formation before going on to disrupt. This HVC could either have an external origin or be re-accreted after an outflow from NGC 247 – with the latter strongly preferred by metallicity considerations. Davidge (2021) suggested HVCs as the triggers for the disc bubbles in NGC 247, and Price-Whelan et al. (2019) suggested an HVC as an alternative origin for PW 1. It is, however, unclear how plausible it is for a low-mass galaxy like NGC 247 to host an HVC with a mass of $\sim 10^8$ M$_\odot$ (as needed to explain the dynamical disturbances).

A third possible scenario is a fly by (not an impact) of a relatively massive satellite galaxy that perturbed the disc of NGC 247 and triggered the formation of SC1 – either in a galactic feather or via an HVC that was shed by the satellite and impacted the disc. The provocateur galaxy would still be visible nearby: assuming a mean relative velocity of ~ 100 km s^{-1}, after 300 Myr the distance travelled would be only ~ 30 kpc. There are two known satellites that might fit this scenario, with three-dimensional (3D) distances to NGC 247 that are constrained by a homogeneous tip of the RGB method (Dalcanton et al. 2009): UGCA 15 (DDO 6) and ESO 540-G032, both with stellar masses of $\sim 3 \times 10^7$ M$_\odot$ and classified as transition-type dwarfs that are gas rich but with recently decreased star formation (Weisz et al. 2011). Their relative velocities and most likely 3D distances are fairly large and suggestive of recent infall on wide orbits, but their minimum distances are compatible with having a recent close approach to NGC 247 – particularly in the case of UGCA 15 (40 kpc). Their stellar metallicities are in the range of [Z/H] ~ -2 to -1.5 (Sharina et al. 2008; Lianou et al. 2013), which suggests they did not shed gas to form SC1 unless there was mixing with NGC 247 disc gas, so the most plausible scenario is that one of them excited a galactic feather in the disc of NGC 247,

A final scenario is that SC1 simply formed in the outer disc of NGC 247, with a satellite interaction as in the previous scenario both triggering the formation of SC1 through a density wave (cf. Bush et al. 2010) and clearing away the requisite gas (which might also have lower metallicity than the main disc).

In summary, we have examined several different scenarios (minor merger, HVC infall, satellite fly by, triggered in-situ formation) that relate the origin of the SC1 complex to other disturbances in NGC 247. If the metallicities of SC1 and the host galaxy disc are indeed the same, then probably the best explanation would be formation in a filament of disc material that was dynamically perturbed. Dynamical models of the interaction could provide further clarification, and more work is also needed on confirming the metallicity of the NGC 247 disc.

5.4 Formation mechanisms of low-density clusters

Given the nature of SC1 as the first clearly identified young FF, we consider briefly how its formation history may connect to its size, and if there are any broader implications for the formation of low-density star clusters. Star cluster formation through galaxy interactions and within tidal debris has been well studied (e.g. Whitmore et al. 1999; Boselli et al. 2018; Fensch et al. 2019), but any

corresponding variations in cluster size have not. The size trends for ordinary GCs are not fully understood, much less those of clusters deviating from the average. GCs are presumed to form from giant molecular clouds (GMCs), which have surface densities of ~ 100– 1000 M$_\odot$ pc^{-2} depending on the galactic environment and the region within the cloud. For a given environment and spatial scale, the GMCs have a near-constant surface density, or equivalently a strong size– mass relation. GCs, on the other hand, have near-constant sizes with surface densities ranging from ~ 100 to 10^4 M$_\odot$ pc^{-2} (e.g. Krumholz, McKee & Bland-Hawthorn 2019). Young clusters appear to bridge this gap between GCs and GMCs, with a size–mass relation that corresponds to a relatively narrow range of surface densities that is strongly peaked around 300 M$_\odot$ pc^{-2} (see lower panel of Fig. 7) and is a fairly universal trend from galaxy to galaxy, despite the host galaxies having a wide range of star formation rates (Brown & Gnedin 2021).

While mechanisms that conspire to decouple GC sizes from their parent GMC sizes remain unclear, the origins of ECs and FFs with densities as low as ~ 10 M$_\odot$ pc^{-2} are even murkier. One tidy explanation for ECs is that some star clusters started out compact but expanded to fill their tidal radii, driven by internal dynamics (e.g. Gieles et al. 2010; Madrid et al. 2012). However, not all clusters fill their tidal radii, and it appears that there is already a difference at birth between compact and ECs (Baumgardt et al. 2010; Hurley & Mackey 2010; Bianchini et al. 2015).

SC1 provides an important example of a massive cluster born large, as it has not lived enough Gyr for the internal expansion processes to take effect. If it is a typical progenitor of old FFs, then it may represent a different formation pathway than for compact star clusters. In addition, the conditions for this pathway would not be ubiquitous, since there are strong differences between galaxies, even of the same type and environment, in how many FFs they host (Peng et al. 2006). The FFs do generally appear associated with galactic discs, and could be considered as massive open clusters, but this still begs the question: Why do discs form some clusters diffuse and some compact? And why do some discs form *only* compact clusters?

One mechanism proposed for the formation of discy systems of FFs is head-on galaxy mergers similar to the Cartwheel (Burkert et al. 2005). The resulting clumpy rings might be conducive to coalescence of small clusters into large, low-density clusters, rather than forming the usual dense progenitors of GCs. Elmegreen (2008) developed a related model that explains FF formation through high Mach numbers in low density gas clouds, such as may be found in collisional rings. NGC 247 is not such an extreme example of a collision, nor of a populous system of FFs (which host ~ 20 objects; Liu et al. 2016), but the localized physical conditions leading to the formation of SC1 may have been similar to those. More generally, SC1 provides fresh evidence that low-density cluster formation is somehow related to galaxy interactions – a scenario that merits further study.

6 CONCLUSIONS

We have discovered and characterized a young faint fuzzy (FF) star cluster, SC1, around the nearby low-mass spiral galaxy NGC 247. This is a rare case of an FF found shortly after formation, providing unique leverage on understanding the origins of low-density star clusters. *HST* analysis of the CMD of SC1, assisted by parallel analysis of simulated cluster observations, indicates an age of $\simeq 300$ Myr and a metallicity of [Z/H] ~ -0.6, based on blue-loop stars with support from the main-sequence turn-off, and where the precision is limited by systematics. The luminosities of the blue loop stars have no significant scatter relative to a simulated population

from the isochrone, placing an upper limit on the age spread of ∼50 Myr. SC1 thus differs from other young and intermediate-age clusters that have been claimed as having larger age spreads – underlining the complexity of piecing together the general puzzle of multiple populations. There are several bright stars with intermediate colours that are associated with SC1 and that are difficult to explain with the single stellar population. One possible explanation is that these are the product of post-main-sequence binary-star mergers.

The estimated stellar mass and size of SC1 are $M_\star = (8.9 \pm 0.5) \times 10^4\ \mathrm{M_\odot}$ and $r_\mathrm{h} = 11.7 \pm 0.5$ pc. SC1 appears to be surrounded by local tidal debris and on larger scales to be associated with structure of the same stellar population age: a low mass ($\sim 10^4\ \mathrm{M_\odot}$) stellar filament that is ∼2 kpc long and that contains two lower mass, relatively large clusters ($M_\star \sim 4000\ \mathrm{M_\odot}$, $r_\mathrm{h} \simeq 5$–6 pc), plus an even larger low-mass cluster ($r_\mathrm{h} \simeq 10$ pc) that may be embedded in the outer disc.

SC1 is close to the outer edge of the host galaxy disc in projection, and has a velocity that is similar to but significantly different from the disc velocity field. Tidal radius arguments suggest that the cluster may be orbiting in the galaxy halo. Whether currently located in the halo or the disc, the question remains of how such a relatively massive cluster of young stars ended up outside of the main star-forming regions of the disc. We consider various explanatory scenarios for both SC1 and its associated stellar filament and low-mass clusters, in conjunction with previous evidence for significant perturbation of the host galaxy. Here a key constraint is that the metallicity of this new material is comparable to, and possibly slightly lower than, the young-disc metallicity.

Although the formation scenarios are still somewhat speculative, two general candidates emerge. First is the origin of the SC1 complex in disc material that was either flung out of the disc by a galaxy interaction as a 'galactic feather,' or was formed in a warped outer disc that subsequently lost much of its gas. Here there may be some tension with the relative metallicities of SC1 and the disc. The second scenario is the passage of a gas-rich UFD galaxy through the disc to produce a gas streamer that was a mixture of dwarf gas and disc gas. This streamer experienced enough shocking to form stars and clusters, and subsequently dispersed. An interesting consequence of this scenario is that the stellar component of the dwarf could still be found lurking relatively intact in the halo, since it typically takes multiple orbits for an infalling satellite to lose all of its dark matter and disperse.

SC1 and its associated lower mass clusters provide new clues to the long-standing mystery of how low-density star clusters are formed. In this case there appears to be a connection to an external perturbation of the host galaxy, which builds on existing ideas that low-density star clusters may form preferentially in low-density regions during galactic interactions.

Various avenues are available to illuminate the origins of SC1 and of ECs and FFs more generally. Further spectroscopic analysis and observations of SC1 and the host galaxy disc could determine if their chemical abundance patterns are the same. Theoretical modeling is needed of the orbit of SC1, of various interaction scenarios, and of the physics of star cluster formation at low densities. Observational surveys of the outer regions of star-forming galaxies and tidal debris could determine if and when low-density young star clusters are prevalent.

ACKNOWLEDGEMENTS

DATA AVAILABILITY

The *HST* and Keck underlying this article are available in MAST and the Keck Observatory Archive, respectively. The Subaru and CTIO data underlying this article will be shared on reasonable request to the corresponding author.

REFERENCES

Ahn C. P. et al., 2018, ApJ, 858, 102
Aihara H. et al., 2018a, PASJ, 70, S4
Aihara H. et al., 2018b, PASJ, 70, S8
Aihara H. et al., 2019, PASJ, 71, 114
Applebaum E., Brooks A. M., Christensen C. R., Munshi F., Quinn T. R., Shen S., Tremmel M., 2021, ApJ, 906, 96
Asa'd R., Hernandez S., As'ad A., Molero M., Matteucci F., Larsen S., Chilingarian I. V., 2022, ApJ, 929, 174
Barmina R., Girardi L., Chiosi C., 2002, A&A, 385, 847
Bastian N., de Mink S. E., 2009, MNRAS, 398, L11
Bastian N., Lardo C., 2018, ARA&A, 56, 83
Baumgardt H., Parmentier G., Gieles M., Vesperini E., 2010, MNRAS, 401, 1832
Bellazzini M., Ibata R. A., Martin N., Malhan K., Marasco A., Famaey B., 2019, MNRAS, 490, 2588
Bianchini P., Renaud F., Gieles M., Varri A. L., 2015, MNRAS, 447, L40
Bigiel F., Leroy A., Walter F., Blitz L., Brinks E., de Blok W. J. G., Madore B., 2010, AJ, 140, 1194
Bosch J. et al., 2018, PASJ, 70, S5
Bosch J. et al., 2019, in Teuben P. J., Pound M. W., Thomas B. A., Warner E. M., eds, ASP Conf. Ser. Vol. 523, Astronomical Data Analysis Software and Systems XXVII. Astron. Soc. Pac., San Francisco, p.521
Boselli A. et al., 2018, A&A, 615, A114
Brodie J. P., Larsen S. S., 2002, AJ, 124, 1410

Brodie J. P., Romanowsky A. J., Strader J., Forbes D. A., 2011, AJ, 142, 199
Brown G., Gnedin O. Y., 2021, MNRAS, 508, 5935
Brüns C. et al., 2005, A&A, 432, 45
Brüns R. C., Kroupa P., Fellhauer M., Metz M., Assmann P., 2011, A&A, 529, A138
Bruzual G., Charlot S., 2003, MNRAS, 344, 1000
Burkert A., Brodie J., Larsen S., 2005, ApJ, 628, 231
Bush S. J., Cox T. J., Hayward C. C., Thilker D., Hernquist L., Besla G., 2010, ApJ, 713, 780
Cadelano M., Dalessandro E., Salaris M., Bastian N., Mucciarelli A., Saracino S., Martocchia S., Cabrera-Ziri I., 2022, ApJ, 924, L2
Carlin J. L. et al., 2016, ApJ, 828, L5
Carlin J. L. et al., 2019, ApJ, 886, 109
Carlin J. L. et al., 2021, ApJ, 909, 211
Cassisi S., Salaris M., 2020, A&A Rev., 28, 5
Choi J., Dotter A., Conroy C., Cantiello M., Paxton B., Johnson B. D., 2016, ApJ, 823, 102
Clough S. A., Shephard M. W., Mlawer E. J., Delamere J. S., Iacono M. J., Cady-Pereira K., Boukabara S., Brown P. D., 2005, J. Quant. Spec. Radiat. Transf., 91, 233
Cockcroft R. et al., 2011, ApJ, 730, 112
Conroy C., Gunn J. E., White M., 2009, ApJ, 699, 486
Cook D. O. et al., 2014, MNRAS, 445, 881
Costa G., Girardi L., Bressan A., Chen Y., Goudfrooij P., Marigo P., Rodrigues T. S., Lanza A., 2019, A&A, 631, A128
D'Ercole A., D'Antona F., Ventura P., Vesperini E., McMillan S. L. W., 2010, MNRAS, 407, 854
Da Costa G. S., Grebel E. K., Jerjen H., Rejkuba M., Sharina M. E., 2009, AJ, 137, 4361
Dalcanton J. J. et al., 2009, ApJS, 183, 67
Davidge T. J., 2006, ApJ, 641, 822
Davidge T. J., 2021, ApJ, 161, 93
Dong H., Calzetti D., Regan M., Thilker D., Bianchi L., Meurer G. R., Walter F., 2008, AJ, 136, 479
Drinkwater M. J., Jones J. B., Gregg M. D., Phillipps S., 2000, PASJ, 17, 227
Duc P.-A. et al., 2015, MNRAS, 446, 120
Dupree A. K. et al., 2017, ApJ, 846, L1
Elmegreen B. G., 2008, ApJ, 672, 1006
Fall S. M., Romanowsky A. J., 2018, ApJ, 868, 133
Fellhauer M., Kroupa P., 2002, MNRAS, 330, 642
Fensch J. et al., 2019, A&A, 628, A60
Fitzpatrick E. L., 1999, PASP, 111, 63
Forbes D. A., Pota V., Usher C., Strader J., Romanowsky A. J., Brodie J. P., Arnold J. A., Spitler L. R., 2013, MNRAS, 435, L6
Forbes D. A., Almeida A., Spitler L. R., Pota V., 2014, MNRAS, 442, 1049
Gaia Collaboration et al., 2018, A&A, 616, A1
Gieles M., Baumgardt H., Heggie D. C., Lamers H. J. G. L. M., 2010, MNRAS, 408, L16
Gieles M., Erkal D., Antonini F., Balbinot E., Peñarrubia J., 2021, Nat. Astron., 5, 957
Gossage S. et al., 2019, ApJ, 887, 199
Goudfrooij P., Girardi L., Correnti M., 2017, ApJ, 846, 22
Grudić M. Y., Kruijssen J. M. D., Faucher-Giguère C.-A., Hopkins P. F., Ma X., Quataert E., Boylan-Kolchin M., 2021, MNRAS, 506, 3239
Grudić M. Y., Hafen Z., Rodriguez C. L., Guszejnov D., Lamberts A., Wetzel A., Boylan-Kolchin M., Faucher-Giguère C.-A., 2022, preprint (arXiv:2203.05732)
Gullikson K., Dodson-Robinson S., Kraus A., 2014, AJ, 148, 53
Hilker M., Infante L., Vieira G., Kissler-Patig M., Richtler T., 1999, A&AS, 134, 75
Hlavacek-Larrondo J., Marcelin M., Epinat B., Carignan C., de Denus-Baillargeon M. M., Daigle O., Hernandez O., 2011, MNRAS, 416, 509
Horne K., 1986, PASP, 98, 609
Hurley J. R., Mackey A. D., 2010, MNRAS, 408, 2353
Huxor A. P., Tanvir N. R., Irwin M. J., Ibata R., Collett J. L., Ferguson A. M. N., Bridges T., Lewis G. F., 2005, MNRAS, 360, 1007
Huxor A. P. et al., 2014, MNRAS, 442, 2165
Hwang N., Lee M. G., 2008, AJ, 135, 1567
Hwang N., Lee M. G., Lee J. C., Park W.-K., Park H. S., Kim S. C., Park J.-H., 2011, ApJ, 738, 58
Janesh W., Rhode K. L., Salzer J. J., Janowiecki S., Adams E. A. K., Haynes M. P., Giovanelli R., Cannon J. M., 2019, AJ, 157, 183
Jennings Z. G. et al., 2015, ApJ, 812, L10
Johnson B. D., Leja J., Conroy C., Speagle J. S., 2021, ApJS, 254, 22
Kacharov N., Neumayer N., Seth A. C., Cappellari M., McDermid R., Walcher C. J., Böker T., 2018, MNRAS, 480, 1973
Kamann S. et al., 2020, MNRAS, 492, 2177
Kannan R., Macciò A. V., Pasquali A., Moster B. P., Walter F., 2012, ApJ, 746, 10
Kelson D. D., Zabludoff A. I., Williams K. A., Trager S. C., Mulchaey J. S., Bolte M., 2002, ApJ, 576, 720
Krumholz M. R., McKee C. F., Bland-Hawthorn J., 2019, ARA&A, 57, 227
Laporte C. F. P., Johnston K. V., Tzanidakis A., 2019, MNRAS, 483, 1427
Larsen S. S., 1999, A&AS, 139, 393
Larsen S. S., 2004, A&A, 416, 537
Larsen S. S., 2009, A&A, 494, 539
Larsen S. S., Brodie J. P., 2000, AJ, 120, 2938
Larsen S. S., Richtler T., 2000, A&A, 354, 836
Larsen S. S., Richtler T., 2006, A&A, 459, 103
Larsen S. S. et al., 2011, A&A, 532, A147 (L11)
Lee M. G., Chandar R., Whitmore B. C., 2005, AJ, 130, 2128
Lelli F., McGaugh S. S., Schombert J. M., 2016, AJ, 152, 157
Lennon D. J. et al., 2018, A&A, 619, A78
Leroy A. K. et al., 2019, ApJS, 244, 24
Li P., Lelli F., McGaugh S., Schombert J., 2020, ApJS, 247, 31
Li C., Tang B., Milone A. P., de Grijs R., Hong J., Yang Y., Wang Y., 2021, ApJ, 906, 133
Lianou S., Grebel E. K., Da Costa G. S., Rejkuba M., Jerjen H., Koch A., 2013, A&A, 550, A7
Liu Y., Peng E. W., Lim S., Jordán A., Blakeslee J., Côté P., Ferrarese L., Pattarakijwanich P., 2016, ApJ, 830, 99
Mackey A. D., Broby Nielsen P., Ferguson A. M. N., Richardson J. C., 2008, ApJ, 681, L17
McLaughlin D. E., van der Marel R. P., 2005, ApJS, 161, 304
Madrid J. P., Hurley J. R., Sippel A. C., 2012, ApJ, 756, 167
Magnier E. A. et al., 2013, ApJS, 205, 20
Marigo P. et al., 2017, ApJ, 835, 77
Martínez-Delgado D. et al., 2012, ApJ, 748, L24
Martinez-Delgado D. et al., 2021, preprint (arXiv:2104.06071)
Mayes R. J., Drinkwater M. J., Pfeffer J., Baumgardt H., Liu C., Ferrarese L., Côté P., Peng E. W., 2021, MNRAS, 506, 2459
Miller Bertolami M. M., 2016, A&A, 588, A25
Milone A. P., Bedin L. R., Piotto G., Anderson J., 2009, A&A, 497, 755
Milone A. P. et al., 2017, MNRAS, 465, 4363
Milone A. P. et al., 2018, MNRAS, 477, 2640
Miyazaki S. et al., 2012, in McLean I. S., Ramsay S. K., Takami H., eds, SPIE Conf. Ser. Vol. 8446, Ground-based and Airborne Instrumentation for Astronomy IV. SPIE, Bellingham, p. 84460Z
Niederhofer F., Georgy C., Bastian N., Ekström S., 2015, MNRAS, 453, 2070
Oke J. B. et al., 1995, PASP, 107, 375
Olsen K. A. G., Miller B. W., Suntzeff N. B., Schommer R. A., Bright J., 2004, AJ, 127, 2674
Ott J. et al., 2012, AJ, 144, 123
Pancino E., 2018, A&A, 614, A80
Pechetti R., Seth A., Neumayer N., Georgiev I., Kacharov N., den Brok M., 2020, ApJ, 900, 32
Peng E. W. et al., 2006, ApJ, 639, 838
Ponomareva A. A., Verheijen M. A. W., Bosma A., 2016, MNRAS, 463, 4052
Price-Whelan A. M., Nidever D. L., Choi Y., Schlafly E. F., Morton T., Koposov S. E., Belokurov V., 2019, ApJ, 887, 19
Prochaska J. et al., 2020, J. Open Source Softw., 5, 2308
Purcell C. W., Bullock J. S., Tollerud E. J., Rocha M., Chakrabarti S., 2011, Nature, 477, 301
Reed B. C., Hesser J. E., Shawl S. J., 1988, PASP, 100, 545
Rich R. M. et al., 2019, MNRAS, 490, 1539
Richtler T., Bassino L. P., Dirsch B., Kumar B., 2012, A&A, 543, A131

Romanowsky A. J., Fall S. M., 2012, ApJS, 203, 17

Ruiz-Lara T., Gallart C., Bernard E. J., Cassisi S., 2020, Nat. Astron., 4, 965

Ryon J. E. et al., 2015, MNRAS, 452, 525

Sahu K., Deustua S., Sabbi E., 2014, WFC3/UVIS Photometric Transformations, Space Telescope WFC Instrument Science Report. STScI, Baltimore

Santhanakrishnan V., 2016, Master's thesis, San Jose State University

Saracino S. et al., 2020, MNRAS, 498, 4472

Schlafly E. F., Finkbeiner D. P., 2011, ApJ, 737, 103

Schlafly E. F. et al., 2012, ApJ, 756, 158

Shah M., Bekki K., Vinsen K., Foster S., 2019, MNRAS, 482, 4188

Sharina M. E. et al., 2008, MNRAS, 384, 1544

Simon J. D., 2019, ARA&A, 57, 375

Stetson P. B., 1987, PASP, 99, 191

Stetson P. B., 1992, in Worrall D. M., Biemesderfer C., Barnes J., eds, ASP Conf. Ser Vol. 25, Astronomical Data Analysis Software and Systems I. Astron. Soc. Pac., San Francisco, p. 297

Stetson P. B., 1994, PASP, 106, 250

Tepper-García T., Bland-Hawthorn J., 2018, MNRAS, 473, 5514

Tonry J. L. et al., 2012, ApJ, 750, 99

Tully R. B. et al., 2013, AJ, 146, 86

van Dokkum P. G., Conroy C., 2012, ApJ, 760, 70

Wagner-Kaiser R., De Maio T., Sarajedini A., Chakrabarti S., 2014, MNRAS, 443, 3260

Wang C. et al., 2022, Nat. Astron., 6, 480

Wechsler R. H., Tinker J. L., 2018, ARA&A, 56, 435

Weisz D. R. et al., 2011, ApJ, 739, 5

Westmeier T. et al., 2017, MNRAS, 472, 4832

Wheeler C. et al., 2019, MNRAS, 490, 4447

Whitmore B. C., Zhang Q., Leitherer C., Fall S. M., Schweizer F., Miller B. W., 1999, AJ, 118, 1551

[1]*Department of Physics & Astronomy, San José State University, One Washington Square, San Jose, CA 95192, USA*

[2]*University of California Observatories, 1156 High Street, Santa Cruz, CA 95064, USA*

[3]*Department of Astronomy & Astrophysics, University of California Santa Cruz, 1156 High Street, Santa Cruz, CA 95064, USA*

[4]*Department of Astrophysics/IMAPP, Radboud University, PO Box 9010, NL-6500 GL Nijmegen, the Netherlands*

[5]*Waterloo Centre for Astrophysics, Department of Physics & Astronomy, University of Waterloo, 200 University Ave. W., Waterloo, Ontario N2L 3G1, Canada*

[6]*Rubin Observatory Project Office, 950 N. Cherry Ave., Tucson, AZ 85719, USA*

[7]*University of Turku, Finnish Centre of Astronomy with ESO (FINCA), Vesilinnantie 5, FI-20014 Turku, Finland*

[8]*Space Physics and Astronomy Research Unit, University of Oulu, PO Box 3000, FI-90014 Oulun yliopisto, Finland*

[9]*Specim, Spectral Imaging Ltd., Elektroniikkatie 13, FI-90590 Oulu, Finland*

[10]*Steward Observatory, University of Arizona, 933 North Cherry Avenue, Tucson, AZ 85721, USA*

[11]*Center for Data Intensive and Time Domain Astronomy, Department of Physics and Astronomy, Michigan State University, East Lansing, MI 48824, USA*

[12]*Centre for Astrophysics and Supercomputing, Swinburne University, John Street, Hawthorn, VIC 3122, Australia*

[13]*School of Physics and Astronomy, RIT, Rochester, NY 14623, USA*

[14]*Institute for Advanced Study, 1 Einstein Drive, Princeton, NJ 08540, USA*

[15]*University of Tampa, 401 West Kennedy Boulevard, Tampa, FL 33606, USA*

[16]*CCAPP and Department of Astronomy, The Ohio State University, 140 W. 18th Ave., Columbus, OH 43210, USA*

[17]*Space Telescope Science Institute, 3700 San Martin Drive, Baltimore, MD 21218, USA*

[18]*Department of Physics, Engineering Physics and Astronomy, Queen's University, Kingston, ON K7L 3N6, Canada*

[19]*Instituto de Astrofísica de Canarias, E-38205 La Laguna, Tenerife, Spain*

[20]*Departamento de Astrofísica, Universidad de La Laguna, E-38205 La Laguna, Tenerife, Spain*

[21]*NSF's National Optical-Infrared Astronomy Research Laboratory, 950 N. Cherry Ave., Tucson, AZ 85719, USA*

[22]*Department of Physics & Astronomy, University of North Carolina at Chapel Hill, 120 E. Cameron Ave, Chapel Hill, NC 27599, USA*

[23]*Royal Military College of Canada, PO Box 17000, Station Forces, Kingston, Ontario, K7K 7B4, Canada*

[24]*Department of Astronomy, Yale University, 52 Hillhouse Avenue, New Haven, CT 06511, USA*

This paper has been typeset from a TEX/LATEX file prepared by the author.